9/1/2015

1 **(Revision)**

2

3 **In defence of Magnetite-Ilmenite Thermometry in the Bishop Tuff and its**

4 **implication for gradients in silicic magma reservoirs**

5

6 BERNARD W. EVANS[1], WES HILDRETH[2], OLIVIER BACHMANN[3],

7 BRUNO SCAILLET[4]

8

9 [1]Department of Earth and Space Sciences, University of Washington, Seattle WA 98195-

10 1310, U.S.A.

11 [2]U.S. Geological Survey, 345 Middlefield Road, Menlo Park, CA 94025, U.S.A.

12 [3]Institute of Geochemistry and Petrology, Department of Earth Sciences, ETH Zurich,

13 Clausiusstrasse 25, 8092 Zurich, Switzerland

14 [4]Institut de Sciences de la Terre d'Orléans, CNRS-Université d'Orléans-BRGM, UMR

15 7327, 1A Rue de la Férollerie, 45100 Orléans, France

16

17

18

19 **ABSTRACT**

20

21 Despite claims to the contrary, the compositions of magnetite and ilmenite in

22 the Bishop Tuff correctly record the changing conditions of $T$ and $fO_2$ in the magma

23 reservoir. In relatively reduced ($\Delta$NNO < 1) siliceous magmas (e.g., Bishop Tuff,

1

9/1/2015

24    Taupo units), Ti behaves compatibly ($D_{Ti} \approx$ 2-3.5), leading to a decrease in $TiO_2$

25    activity in the melt with cooling and fractionation. In contrast, FeTi-oxides are

26    poorer in $TiO_2$ in more oxidized magmas ($\Delta$NNO > 1, e.g., Fish Canyon Tuff,

27    Pinatubo), and the $d(a TiO_2)/dT$ slope can be negative. Biotite, FeTi-oxides, liquid,

28    and possibly plagioclase largely maintained equilibrium in the Bishop Tuff magma

29    (unlike the pyroxenes, and cores of quartz, sanidine, and zircon) prior to and during

30    a mixing event triggered by a deeper recharge, which, based on elemental diffusion

31    profiles in minerals, took place at least several decades before eruption.

32    Equilibrating phases and pumice compositions show evolving chemical variations

33    that correlate well with mutually consistent temperatures based on the FeTi-oxides,

34    sanidine-plagioclase, and $\Delta^{18}$O quartz-magnetite pairs. Early Bishop Tuff (EBT)

35    temperatures are lower (700 to ~780°C) than temperatures (780 to >820°C)

36    registered in Late Bishop Tuff (LBT), the latter defined here not strictly

37    stratigraphically, but by the presence of orthopyroxene and reverse-zoned rims on

38    quartz and sanidine. The claimed similarity in compositions, Zr-saturation

39    temperatures and thermodynamically calculated temperatures (730-740°C)

40    between EBT and less evolved LBT reflect the use of glass inclusions in quartz cores

41    in LBT that were inherited from the low temperature rhyolitic part of the reservoir

42    characteristic of the EBT. LBT temperatures as high as 820°C, the preservation of

43    orthopyroxene, and the presence of reverse-zoned minerals (quartz, sanidine,

44    zircons) are consistent with magma recharge at the base of the zoned reservoir,

45    heating the cooler rhyolitic melt, partly remelting cumulate mush, and introducing

9/1/2015

46    enough $CO_2$ (0.4-1.4 wt%, mostly contained in the exsolved fluid phase) to

47    significantly lower $H_2O$-activity in the system.

48

49    Key words: Bishop Tuff, ilmenite-magnetite thermometry, $TiO_2$ activity,

50    reduced magmas, "bright rims", melt inclusions, magma recharge, $CO_2$ effect.

51

52                                  **INTRODUCTION**

53

54    Among large-volume silicic eruptions, the Bishop Tuff (Long Valley caldera,

55    California) has received unusual attention from workers interested in issues such as

56    magma chamber dimensions, longevity, temperatures, depths, compositions,

57    differentiation processes, magma mixing and eruption history (dozens of papers

58    since Hildreth 1977; Hildreth 1979; Hildreth 1981). Nonetheless, controversy

59    remains with regard to the pre-eruption temperature gradient of the Bishop Tuff

60    magma. Taken at face value the ilmenite-magnetite thermometer records a

61    continuous span in temperature from about 700 to 820°C and in $fO_2$ from $\Delta$NNO = -

62    0.5 to +0.5 log units (Hildreth and Wilson 2007; Ghiorso and Evans 2008), between

63    respectively highly evolved, crystal-poor rhyolitic pumice and less evolved, crystal-

64    rich pumice. The accuracy of these temperatures has been challenged in several

65    communications (Frost and Lindsley 1991; Ghiorso and Sack 1991; Lindsley et al.

66    1991; Frost and Lindsley 1992; Ghiorso and Evans 2008), and most recently by

67    Ghiorso and Gualda (2013), Gualda and Ghiorso (2013b) and Gardner et al. (2014).

68    These authors have concluded that ilmenite was not everywhere in equilibrium with

3

9/1/2015

69   the magnetite, so that the compositions of the oxide pair do not accurately preserve

70   a record of intensive variables such as pre-eruptive $T$ and $fO_2$ in the magma

71   reservoir.

72       There is scarcely any more important parameter needed for an enlightened

73   understanding of a giant volcanic system than the spatial and temporal variation of

74   temperature in the magma chamber, as customarily witnessed by the erupted and

75   quenched products. We will try to show in this paper that the widely used FeTi-

76   oxide thermobarometer is reliably linked to Bishop Tuff magma-chamber

77   conditions, supported as it is by $\Delta^{18}O$ quartz-magnetite, two-feldspar, and Zr-

78   saturation thermometry, and laboratory phase-equilibrium constraints. Our view is

79   consistent with the early classical studies of the Bishop Tuff by Wes Hildreth as well

80   as several recent contributions (Hildreth and Wilson 2007; Wark et al. 2007; Evans

81   and Bachmann 2013; Roberge et al. 2013; Chamberlain et al. 2014a; Chamberlain et

82   al. 2014b; Chamberlain et al. 2015).

83

84                     **COMPOSITIONAL RANGE OF THE BISHOP TUFF**

85

86   **Compositional Continuity**

87

88       About 95% of the Bishop Tuff consists of a compositional continuum from

89   crystal-poor to crystal-rich rhyolitic pumice, and ~5% is crystal-poor dark and

90   swirly pumice (Fig. 1). There are also very rare crystal-rich pumices of trachydacite

91   and trachyandesite composition. The more evolved crystal-poor pumice and the less

4

9/1/2015

92   evolved crystal-rich pumice were erupted early and throughout the eruptive

93   sequence in most outflow sectors. The respective stratigraphic predominance of

94   crystal-poor and crystal-rich pumice types led to the simplification early (EBT) vs.

95   late Bishop Tuff (LBT) introduced by Hildreth (1979) as a useful device to contrast

96   the compositional features of the Bishop Tuff array. We stress, however, that it does

97   not reflect a *compositional bimodality* in magma compositions (Hildreth and Wilson

98   2007).

99        The "standard" model for the Bishop Tuff involves sequential eruption from

100  progressively deeper portions of a single compositionally and thermally stratified

101  magma chamber, resulting in inversion of the stratigraphy (Hildreth 1977, 1979;

102  Wilson and Hildreth 1997; Hildreth and Wilson 2007; Roberge et al. 2013;

103  Chamberlain et al. 2015). Gualda and Ghiorso (2013a) challenged this model on the

104  basis of perceived compositional bimodalities and substituted a model involving

105  two magma chambers.

106       The continuity of geological, mineralogical, and geochemical properties of the

107  Bishop Tuff eruption, and their connection to the eruptive sequence, were

108  summarized in Hildreth and Wilson (2007). These continua are manifested by

109  progressive changes in pumice-type proportions, crystal content of pumices, major-

110  and trace-element pumice compositions, and mineral and matrix-glass compositions

111  (Figs. 2-5). We do not find gaps in plots of these datasets of a magnitude that, given

112  known sampling constraints, would lead us to entertain the idea of eruptions from

113  two (or more) separate reservoirs. Fig. 2 typifies the continuity in whole-rock

114  compositions (WR, all from single pumice clasts) for Ti and Ba in the Bishop Tuff.

5

9/1/2015

115    Likewise, Roberge et al. (2013) demonstrated the compositional continua of matrix

116    glass and melt inclusions across the early/middle/late Bishop Tuff array. In a

117    comprehensive major- and trace-element study of crystals and matrix glass,

118    Chamberlain et al. (2015) reinforce these relationships among phase compositions,

119    sample locations, stratigraphy, and magma evolution.

120        The idea of bimodality was unintentionally supported by studies that

121    focussed on a small number of samples clearly recognized as early vs. late erupted

122    parts of the sequence (e.g., Anderson et al. 2000). However, the far more abundant

123    sampling tabulated and plotted in Hildreth and Wilson (2007) remedied the

124    apparent data gaps for intermediate WR and FeTi-oxide compositions. For example,

125    the cation ratios Mg/(Mg+Fe) of the two FeTi-oxides (Fig. 3) vary continuously

126    across the "main suite" (which contains the "normal" as distinct from the "variant"

127    pumice type, Hildreth and Wilson 2007, Table 1) and coherently with each other

128    (Evans and Bachmann 2013). Frequency maxima (Fig. 3) close to the evolved low-

129    $X_{Mg}$ (and low-$T$) extremes are also a feature of the WR compositions (Hildreth and

130    Wilson 2007). These maxima reflect the fact that crystal-poor pumices of units Ig1

131    and F1-8 (Fig. 1) make up 2/3 or more of the eruptive volume accessible to

132    sampling, and they are more easily sampled than pumices from the overlying Ig2

133    and F9 units. This effect shows up very clearly in the frequency histograms for

134    whole-rock Ba and Sr (Fig. 4). Samples of late Bishop Tuff (as defined below)

135    account for less than one-quarter of the accessible eruptive volume. Most of the

136    compositional *range* in the main suite of pumice in the Bishop Tuff occurs in the Ig2

137    units.

6

9/1/2015

138

**Early and Late Bishop Tuff**

140

141      We believe that the most useful usage of the labels Early and Late Bishop Tuff

142    (EBT and LBT) should refer to the absence in the former, and presence in the latter,

143    of quartz with Ti-enriched rims, and sanidine margins enriched in Ba and Sr. The

144    presence of these "reverse" rim features, which are respectively bright in

145    cathodoluminescence (CL) and electron backscatter (EBS) images, implies that LBT

146    experienced a significant, late-magmatic event. Although pumice with bright-

147    rimmed minerals is most commonly present in the temporally late sequence, that is,

148    in Ig2 units (Fig. 1), these features can also be found in earlier erupted pumice; thus,

149    a stratigraphic subdivision of EBT and LBT is less precise. Similarly, LBT pumice

150    tends to be relatively crystal-rich, but crystal-rich pumice is in fact also present

151    throughout the eruptive sequence (Fig. 1). Furthermore, it has become clear over

152    the years that reversely-zoned sanidine and quartz are largely found together with

153    pyroxenes. These are recognized only among the "normal crystal-rich pumice" that

154    increase greatly in abundance later in the eruptive sequence (Fig. 1). Averages of

155    EBT and LBT pumice compositions (Table 1) show the former to be compositionally

156    more evolved than the latter.

157      The bright rims of quartz and sanidine phenocrysts in LBT, outboard of a

158    resorption surface, are enriched Ti, Ba, Sr, and LREE, and so, with $CO_2$, are their melt

159    inclusions (Hervig and Dunbar 1992; Wallace et al. 1999; Anderson et al. 2000;

160    Peppard et al. 2001; Roberge et al. 2013). The margins of zircon crystals in LBT are

7

9/1/2015

161    similarly enriched in compatible elements and LREE and depleted in U and Th

162    (Chamberlain et al. 2014b). These crystal rims grew by their envelopment in less

163    evolved, hotter (Chamberlain et al. 2014a) and drier LBT magma (see below). The

164    central "dark" parts of quartz and sanidine in samples of LBT have evolved chemical

165    characteristics similar to EBT quartz and sanidine (low Ti and Ba respectively, and

166    similar melt-inclusion compositions), suggesting their derivation from the EBT

167    magma. We can tell from their major and most trace element compositions that by

168    far the preponderance of analyzed melt inclusions in quartz (91 out of 98; from

169    Wallace et al. 1999; Anderson et al. 2000; Peppard et al. 2001) fall into this inherited

170    "dark core" category (Fig. 2). As discussed below, these observations are critical for

171    the assessment of WR compositions and in attempts to use the compositions of melt

172    inclusions for thermometry and barometry.

173

174                                    **THERMOBAROMETRY**

175

176    **Magnetite-Ilmenite Thermometry**

177

178            The continuity and covariation among observable properties of the Bishop

179    Tuff, including the minerals, was already noted by Hildreth (1977, 1979). The

180    compositions of the FeTi-oxide minerals, and the temperatures they indicated,

181    figured prominently in this narrative. For example, Hildreth (1979) showed the

182    existence of a correlation in the Bishop Tuff between the composition of plagioclase

183    and the FeTi-oxide temperature, with the mean composition of plagioclase varying

8

9/1/2015

184    continuously from $An_{14}$ in cool EBT to $An_{23}$ in hotter LBT. Hildreth (1979) showed

185    that compatible elements such as Ca, Ba, and Eu in sanidine, Ba, Ce and Eu in

186    plagioclase and Ti, Ba, V and Co in biotite all decline with decrease in the FeTi-oxide

187    temperature. Correlated, temperature-dependent changes in the compositions of

188    apatite and zircon were also noted (Hildreth 1979). FeTi-oxide temperatures also

189    correlated well with WR major- and trace-element compositions (Hildreth 1979).

190    Notably, the oxide temperatures were shown by Hildreth (1979) to decline with

191    *increase* in incompatible elements (Mn, Cs, Sc, Yb, Ta, U, Y, Rb) and with *decrease* in

192    compatible elements (Mg, Fe, Ca, Ti, P, Ba, Ce, Eu, Zr, Sr).

193         Hildreth and Wilson (2007) supplied an expanded database of FeTi-oxide

194    compositions and XRF whole-rock analyses for all units of the Bishop Tuff. The FeTi-

195    oxide data were collected by microprobe from pairs of homogeneous grains in

196    mutual contact (Hildreth and Wilson 2007). Use of the revised calibration of the

197    ilmenite-magnetite thermometer of Ghiorso and Evans (2008) with this expanded

198    database (Fig. 5) reinforces Hildreth's (1977, 1979) observations that higher

199    concentrations of compatible elements (Ca, Ti, Fe, Ba) correspond to higher oxide

200    temperatures, and conversely so for the incompatible elements (e.g., Si, Rb). FeTi-

201    oxide temperatures appear  to be accurate to about ± 30-40°C (e.g., Blundy and

202    Cashman 2008), and analytically reproduceable to 5-10°C, provided that instances

203    of inhomogeneity, oxyexsolution, and alteration are avoided. If the composition of

204    ilmenite in the Late Bishop Tuff was largely arrived at syn- or post-eruptively (for

205    example, Gualda and Ghiorso 2013a; Gualda and Ghiorso 2013b; Gardner et al.

206    2014; see below), we fail to see how or why this event could restore/reproduce the

9

9/1/2015

207    relationships between the allegedly incorrect oxide temperatures and magma

208    chemistry that are shown in Fig. 5.

209        Given our definition of LBT (presence of reverse-zoned "bright rim"

210    minerals) and especially the roles of high Ba and Ti, samples of LBT are likely to

211    have Fe-Ti oxide temperatures (Fig. 5) higher than ~780°C and whole-rock (WR)

212    $SiO_2 < 76$ wt%, total FeO > 1.0 wt%, CaO > 0.75 wt%, $TiO_2 > 0.15$ wt%, and Ba > 300

213    ppm. We note that the LBT sample population is limited; bright-rim material may

214    make up only ~ 10% of the (accessible) pumice, i.e., less than half the pumice in Ig2,

215    which is itself only 20-33% of the whole accessible volume.

216        Concern about the validity of the FeTi-oxide temperatures in the Bishop Tuff

217    surfaced when petrologic analysis of the ilmenite-magnetite-orthopyroxene-quartz

218    assemblage gave widely varying and unrealistic results for pressure (<0 to 5 kbar;

219    Frost and Lindsley 1991; Ghiorso and Sack 1991; Lindsley et al. 1991; Frost and

220    Lindsley 1992). Much later, Evans and Bachmann (2013) illustrated the inherited

221    nature of most of the pyroxenes in the Bishop Tuff with the aid of a Roozeboom

222    diagram showing inconsistent Fe/Mg exchange relations between the pyroxenes

223    and FeTi-oxides. It seems, in retrospect, that the comparative homogeneity of the

224    pyroxenes was the problem for which the evolving oxide minerals, specifically the

225    ilmenite, received the blame.

226        A further apparent stumbling block was how to reconcile the roughly 100°C

227    thermal gradient inferred from the FeTi-oxides with the quartz-sanidine-plagioclase

228    "eutectic" nature of the Bishop Tuff throughout (Ghiorso and Evans 2008, p. 1021).

229    This question can be resolved (discussed under "Role of $CO_2$" below) when account

10

9/1/2015

230  is taken of the lower $H_2O$-activity of the LBT magma related to the presence of $CO_2$

231  in the system and/or the partial remelting of dry cumulate crystals (Wolff et al., in

232  press). Finally, Ghiorso and Gualda (2013) argued that the positive slope of the

233  Bishop Tuff oxides in a diagram of derived $aTiO_2$ vs. $T$ is thermodynamically

234  problematic, and therefore the oxide pair were not to be considered in equilibrium.

235  The pitfalls of this conclusion are also addressed below.

236      The irony of the condemnation of the FeTi-thermobarometer in the case of

237  the Bishop Tuff is that the tightness of clustering of most of the datapoints in graphs

238  of $X_{usp}$ vs. $X_{ilm}$ and $\Delta NNO$ vs. $T°C$ is almost unsurpassed by comparable data from

239  other well-studied volcanic centers (e.g., Ghiorso and Evans 2008). The consistency

240  of Mg/Fe partitioning in the Bishop Tuff among ilmenite, magnetite, and biotite

241  (Evans and Bachmann 2013) is supported by the range (570-900°C) in derived

242  MgFe-temperatures (Ghiorso and Evans 2008) that is not notably larger than

243  several other volcanic centers. Fe/Ti exchange is in principle independent of Fe/Mg

244  exchange, and so taken together, despite their very different kinetics, these

245  indications of exchange equilibria provide feeble support for a lack of chemical

246  communication between the ilmenite and the magnetite in samples of LBT (cf.

247  Gualda and Ghiorso 2013a).

248      Three-fold changes in $X_{Mg}$ in both magnetite and ilmenite (Evans and

249  Bachmann 2013) match increases in the magma $X_{Mg}$ from approximately 0.1 to 0.3

250  (Hildreth and Wilson 2007) in the main suite of white pumices from EBT to LBT

251  (crystal-poor, crystal-medium and crystal-rich). These compositional variations are

252  produced by a magma differentiation process that is (largely?) driven by

11

9/1/2015

253    temperature change. Their mutual consistency when plotted against temperature

254    (Fig. 6) suggests strongly that the FeTi-thermometer is accurately recording the

255    process. Similarly, magnetite and ilmenite undergo nearly identical ten-fold

256    increases in Mn/Mg ratio in response to magma evolution from 850°C down to

257    700°C. The ratio Mn/Mg in WR pumice also increases by an order of magnitude over

258    the same range in temperature (although with Mg at the detection limit in evolved

259    samples, the exact degree of change is hard to specify). Again, these internally

260    consistent changes in mineral and pumice compositions as a function of FeTi-

261    temperature are inconsistent with the view that the extracted temperatures are not

262    to be trusted. We do acknowledge, however, that among the 111 analyzed ilmenite-

263    magnetite pairs in the Bishop Tuff, we can identify a small number (3-5) that

264    noticeably fail to conform to the smooth composition/temperature trends shown by

265    the remainder (Figs. 6 and 7). In our view, these few analyses represent the extent

266    to which the oxide minerals, notably the ilmenite, have been influenced by syn- or

267    post-eruption processes.

268        Because $X_{usp}$ of the magnetite is relatively constant at about 0.26 (Frost and

269    Lindsley 1992; Ghiorso and Evans 2008), variation in the $TiO_2$ content of ilmenite is

270    recognized as driving the $fO_2 - T$ trend in the Bishop Tuff oxides. Ghiorso and Gualda

271    (2013) and Gualda and Ghiorso (2013a) maintain that this feature of the trend is a

272    consequence of late- to post-magmatic alteration or formation of the modally small

273    amounts of ilmenite, so that the compositions of the oxide pair do not accurately

274    reflect magma chamber conditions. However, this interpretation of FeTi-exchange

275    disequilibrium is hard to reconcile with the evidence for the preservation of Mg/Fe

12

9/1/2015

276    and Mg/Mn exchange equilibrium among ilmenite, magnetite, and liquid magma

277    discussed above.

278        Whereas the Mg/Fe and Fe-Ti exchange temperatures for the Bishop Tuff fall

279    in the same range, we do not share the enthusiasm of Gardner et al. (2014) for the

280    new and as yet minimally tested Mg/Fe-thermometer for ilmenite-magnetite pairs.

281    By contrast, the experimentally calibrated and independently tested (Ghiorso and

282    Evans 2008; Blundy and Cashman 2008) FeTi-thermometer is more reliable. As

283    expected, Mg/Fe exchange between magnetite and ilmenite proves to be less

284    sensitive to temperature than the Fe-Ti thermometer, and they correlate poorly

285    (slope $m$ = 0.62, $R^2$ = 0.185). The poor correlation between Mg/Fe and Fe-Ti

286    exchange temperatures can be attributed to the larger uncertainties in the Mg/Fe

287    thermometer (as noted in "ctserver.ofm-research.org"), the sources of which are

288    analytical and theoretical. Concentrations of MgO in the oxides in Bishop Tuff

289    pumice are small: in ilmenite 0.59 – 1.8 wt% and in magnetite 0.22 – 0.80 wt%. Also,

290    it is necessary to partition $Fe^{2+}$ and $Fe^{3+}$ from total Fe based on spinel and

291    rhombohedral-oxide formula proportions. MgFe-partitioning between ilmenite and

292    magnetite is not pronounced (Fig. 6), whereas the partitioning of $Fe^{2+}Ti(Fe^{3+})_{-2}$ is

293    strong: 600-800°C isotherms are close to the x- and y-axes of the Roozeboom plot

294    (Ghiorso and Evans 2008). Accordingly, the standard Gibbs energy and enthalpy of

295    Fe-Ti exchange are predictably larger than those for Mg/Fe exchange, so the former

296    thermometer has a stronger dependence of the equilibrium constant $\ln K_{ex}$ on

297    inverse temperature. A quantitative thermodynamic analysis of $Fe^{2+}$-Mg exchange

298    between ilmenite and magnetite in the Bishop Tuff was published as Fig. 25 in

13

9/1/2015

299    Ghiorso and Evans (2008). As for Fe/Mg, the partition of Mn and Mg between

300    magnetite and ilmenite is not useful as a geothermometer. Figure 6 shows that the

301    partitioning is small. The raw $K_d$ or $\ln K_d$ for Mn/Mg exchange correlate poorly ($R^2$ =

302    0.185 and 0.153 respectively) with the FeTi-exchange thermometer.

303         Gardner et al. (2014) criticized our use of Roozeboom and Nernst diagrams

304    to examine exchange equilibrium among coexisting minerals (Evans and Bachmann,

305    2013). We defend their use while freely admitting that they only test exchange

306    equilibrium and do not prove it quantitatively, namely that: "the chemical potential

307    difference of the exchange reaction...is zero over the inferred temperature range of

308    interest" (Gardner et al. 2014, p. 13). Conversely, the diagrams reliably show

309    instances of disequilibrium, as we have noted for the pyroxenes (Evans and

310    Bachmann 2013).

311         Support of a different kind for the validity of the Fe-Ti oxide temperature

312    estimates in the Bishop Tuff was provided by Anderson et al. (2000): "Some

313    pyroxene-bearing LBT samples contain two populations of titaniferous magnetite

314    (both with $X_{usp}$ = 0.26), low-Mg titaniferous magnetite as inclusions in quartz and

315    higher-Mg titaniferous magnetite as individual grains within (matrix) glass. The

316    latter approach Fe-Mg exchange equilibrium with the pyroxenes." These statements

317    are consistent with low-Mg, evolved magnetite inside EBT (antecryst) quartz, and

318    later growth of high-Mg magnetite from less evolved LBT matrix liquid following a

319    recharge event.

320

321    **TiO$_2$ Activity**

14

9/1/2015

322

323       Ghiorso and Gualda (2013) showed that the solubility of rutile in magmatic

324   liquids declines, as expected, with decreasing temperature, so that the slope of a

325   graph of the activity of $TiO_2$ vs. $T$°C based on the compositions of coexisting ilmenite

326   and magnetite in a magma whose composition does not vary appreciably should

327   ordinarily have a negative slope. This assumption seemed reasonable in light of $TiO_2$

328   values of 0.08 and 0.09 wt% adopted for EBT and LBT liquids respectively, based on

329   the average compositions of melt inclusions (MI) in quartz phenocrysts (Anderson

330   et al. 2000). However, as discussed above, we strongly suspect that the MI used by

331   Ghiorso and Gualda (2013) largely represent *highly evolved* EBT compositions, not

332   the extremes of liquid composition corresponding to the analyzed FeTi-oxide

333   minerals in the Bishop Tuff. We present here (Fig. 7) a revised version of Fig. 4 in

334   Ghiorso and Gualda (2013) based on what we feel are more likely liquid

335   compositions matching the 700 and 800°C oxide temperatures.

336       Measured Ti contents of MI in cores and rims of LBT quartz (Fig. 2) were

337   found to range from 353 to 786 ppm ($TiO_2$ from 0.06 to 0.13 wt%) by Wallace et al.

338   (1999), Anderson et al. (2000) and Peppard et al. (2001). Elements in MI trapped in

339   bright overgrowths were shown to be less evolved than MI in dark interiors

340   (Peppard et al. 2001; Roberge et al. 2013). Chamberlain et al. (2015) analyzed

341   matrix glasses in main-suite Bishop Tuff pumice and found Ti contents ranging from

342   less than 400 to as much as 970 ppm when averaged according to stratigraphic unit.

343   In relative proportions, this range is not unlike that found for Ti in Bishop Tuff

344   quartz by Wark et al. (2007). The *overall* range of Ti analyses in main-suite matrix-

15

345    glass samples reported by Chamberlain et al. (2015) is larger, namely from 310 to

346    1280 ppm (0.05 to 0.21 wt% $TiO_2$); five samples of EBT averaged 407-416 ppm Ti

347    (0.07 wt% $TiO_2$). Whole-rock (WR) $TiO_2$ in the FeTi-thermometer population ranges

348    from 0.07 to 0.22 wt%, a 3-fold change (Fig. 5); the WR values for LBT are likely to

349    be as much as 0.045 wt% $TiO_2$ larger than matrix glass owing to the presence of

350    ⌐0.5% magnetite (Hildreth and Wilson 2007). In light of the above, rather than 0.09

351    wt% $TiO_2$, we prefer to select a more likely 0.18 wt% for the LBT matrix liquid

352    matching the 800°C oxide temperature; and rather than 0.08 wt% $TiO_2$, we believe

353    a figure of 0.07 wt% best represents EBT matrix liquid corresponding to the lowest

354    (700°C) temperature. If, accordingly, we adjust the MELTS-derived curve of *aTiO₂*

355    vs. *T*°C for Bishop Tuff rhyolite in Ghiorso and Gualda (2013, their Fig. 4) to fit these

356    preferred estimates of liquid composition (a conservative enrichment factor of

357    0.18/0.07⌐2.5 between the EBT and LBT), we recover a line with a low-angle

358    *positive* slope (Fig. 7). Our adjustment assumes Henry's Law behavior of $TiO_2$ in the

359    liquid. Why our adjusted line is 0.2 units of *aTiO₂* lower than the measured FeTi-

360    oxide data-set for the Bishop Tuff is unclear, but we suspect it is a thermodynamic

361    rather than disequilibrium problem.

362       A comparison of Figures 1 and 2 in Ghiorso and Gualda (2013, *ΔNNO* vs. *T*°C

363    and *aTiO₂* vs. *T*°C respectively) shows that negative-sloped trends of *aTiO₂* vs. *T*°C

364    data-points in their Figure 2 are a property of relatively oxidized intermediate to

365    silicic magmas (*ΔNNO* > 1), whereas positive-sloped data points correspond to

366    reduced magmas (*ΔNNO* < 1). FeTi-oxide minerals in the reduced magmas are Ti-

367    rich (Ghiorso and Evans 2008; namely $X_{usp}$ = 0.2 - 0.6 and $X_{ilm}$ = 0.75 – 0.93), whereas

16

9/1/2015

368    in more oxidized magmas, they are Ti-poor: $X_{usp}$ < 0.2 and $X_{ilm}$ < 0.7, so the

369    compatibility differences for Ti in these magmas are somewhat predictable. We

370    calculate here (Table 2) a partition coefficient $D_{Ti}$ of 2-3.5 for the Bishop Tuff magma

371    with modal proportions given in Hildreth (1977, Appendix XII). These calculations

372    of $D_{Ti}$ are obviously rough because the modal proportions of magnetite and ilmenite

373    are nearly impossible to measure separately, but the results are borne out by the

374    measured temperature dependence of whole-rock $TiO_2$ (Fig. 5), the $TiO_2$ vs. $SiO_2$

375    variation diagram (Hildreth and Wilson 2007, their Fig. 9), and the calculated Ti

376    enrichment factor of ≈74% (Hildreth 1979; Wolff et al. in press). Thus, fractional

377    crystallization of the FeTi-oxides can be expected to deplete Ti in the residual liquid

378    of reduced magmas such as the Bishop Tuff, with somewhat less Ti-depletion in the

379    residual liquid in the case of more oxidized magmas such as the Pinatubo and

380    Shiveluch lavas.

381        Such behavior was experimentally confirmed at $fO_2$ of ΔNNO = 0 to -1.0 log

382    units by Klimm et al. (2003, 2008), using rhyolitic compositions with 0.55, 0.38, and

383    0.17 bulk $TiO_2$ contents (wt%), thus comparable to the full spectrum of Bishop Tuff

384    pumice. For a relatively evolved composition such as AB421 (Table 1), FeTi-oxide

385    saturated residual liquids have $TiO_2$ contents of about 0.15 wt% at 800°C, whereas

386    at 700°C, $TiO_2$ has fallen to 0.06 wt% (Fig. 8). This covariation of  temperature and

387    melt $TiO_2$ content is identical to that displayed by the Bishop Tuff. The flattened

388    trend of AB421 above 800°C in Fig. 8 reflects the fact that this magma is above its

389    liquidus.

17

9/1/2015

390        The contrasting positive and negative slopes for $aTiO_2$ vs. $T°C$ are thus a

391        reflection of magmatic differentiation trends that differ in their igneous

392        compatibility of Ti. In the Bishop Tuff, crystal–liquid fractionation produced the

393        highly evolved, *crystal-poor* EBT pumice (Hildreth and Wilson 2007), but magma

394        mixing and cumulate melting at deeper levels likely contributed to the overall

395        compositional diversity as well (see IMPLICATIONS section). In our view, Ghiorso

396        and Gualda (2013) (and Thomas and Watson 2012) underestimate the influence of

397        magmatic differentiation on the trend of variation of $TiO_2$-activity with temperature.

398        We also note that biotite in the Bishop Tuff shows a *positive* correlation between its

399        $TiO_2$ content and the FeTi-oxide temperature (Hildreth 1979). This calls for a basic

400        exchange-equilibrium control of the compositions of both biotite and ilmenite.

401        The $T – fO_2$ trends for the Bishop Tuff and the similarly reduced Taupo oxides

402        fall very close to one another (Ghiorso and Gualda 2013). Rhyolites from the

403        Oruanui eruption, Taupo Volcano, New Zealand, show about the same relative

404        decline in whole-rock wt% $TiO_2$ as the Bishop Tuff, from 0.42 to 0.16, as $SiO_2$

405        (anhydrous) increases from 76 to 79 wt% (Wilson et al. 2006). The positive slope of

406        $aTiO_2$ vs. $T$ for such reduced magmas is not a "thermodynamic inconsistency"

407        (Gualda and Ghiorso 2013a). It is a petrologic requirement of magmatic

408        differentiation in reduced magmas wherein the cooling trend is *away* rather than

409        towards rutile saturation, that is, a "compositional" as much as a "thermodynamic"

410        control. If the Bishop Tuff oxides are out of equilibrium, then so are the Taupo and

411        the Yellowstone oxides (Ghiorso and Gualda 2013), which pass the Mn/Mg partition

412        test (Bacon and Hirschmann 1988). Oxide temperatures extracted from

18

9/1/2015

413    cummingtonite-bearing Taupo rhyolites were shown (Ghiorso and Evans 2008, Fig.

414    28) to be in agreement with those from other cummingtonite-bearing volcanics and

415    the amphibole quadrilateral phase diagram. It is thus inappropriate in our opinion

416    to condemn the veracity of the FeTi-oxide thermobarometer for the Bishop Tuff (or

417    any other reduced metaluminous magma) on the basis of a positive slope for $aTiO_2$

418    vs. *T.*

419

420    **Other Thermometers**

421        Other thermometers applied to the Bishop Tuff deposits are discussed below.

422    Notwithstanding their different kinetics, they all agree with the ilmenite-magnetite

423    thermometer in showing that EBT and LBT magmas record respectively low and

424    high temperature, and thus the Bishop Tuff magma reservoir was thermally zoned

425    prior to its eruption:

426        1. The $\Delta^{18}O$ quartz-magnetite thermometer applied to EBT and LBT

427            pairs gave a temperature range of 715 to 815°C (Bindeman and Valley

428            2002). This range is remarkably close to that indicated by FeTi-oxide

429            thermometry (Figs. 5, 6, 7).

430        2. A temperature difference of ⬚ 80°C (740-820°) between the earlier-

431            and later-erupted regions of the magma chamber was determined by

432            Chamberlain et al. (2014a) for host-and-inclusion pairs of sanidine

433            and plagioclase. All inclusions measured were within the BSE-dark

434            cores of sanidine crystals, so this range in temperature may be a

435            minimal one for the entire suite according to our definition of LBT.

19

9/1/2015

436      Their two-feldspar temperatures show a positive correlation with Fe-

437      Ti oxide temperatures (their Fig. 2).

438   3   Ti in quartz thermometry (TitaniQ) showed a range from ~720 to

439      820°C on the assumption of a constant activity of 0.6 for $TiO_2$ in the

440      liquid (Wark et al. 2007). Whereas the experimental calibration used

441      by Wark et al. (2007) has been supported by more recent work

442      (Thomas et al. 2015), there remains the need to recognize that $a(TiO_2)$

443      varies with temperature and liquid composition (Ghiorso and Gualda

444      2013). $TiO_2$ activity can in principle be determined from the $TiO_2$

445      contents of nearby melt inclusions and from the compositions of FeTi-

446      oxide in the same sample (assuming they are in frozen equilibrium).

447      This problem is a practical matter that future work may well resolve.

448   4   Gualda and Ghiorso (2013a) found that average zircon-saturation

449      temperatures (735 ± 16 and 735 ± 23°C) were identical in EBT and

450      LBT pumices. These results were based on the Zr contents of glass

451      inclusions in quartz using analytical data from Wallace et al. (1999),

452      Anderson et al. (2000), and Peppard et al. (2001), and the

453      experimental calibration of Watson and Harrison (1983). Only seven

454      of the 97 spots in the analyzed population have more than 80 ppm Ba.

455      Hence it appears that at least 90 % of the analyses represent EBT and

456      that they are from melt inclusions inside the "dark" interiors of

457      quartz. 735°C is not significantly different from the average

458      temperature (728 ± 19°C s.d.) given by the oxide thermometer of

20

9/1/2015

459          Ghiorso and Evans (2008) for 42 EBT pumices identified by their low

460          contents of Ba and Ti (Fig. 2). Gualda and Ghiorso (2013a) mentioned

461          that melt in quartz rims is somewhat enriched in Zr relative to melt in

462          crystal interiors, citing one result (120 ppm Zr) from Peppard et al.

463          (2001) that is equivalent to 765°C. However, Gualda and Ghiorso

464          (2013a, p. 762) are dismissive of quartz-rim MI because "...these

465          inclusions were trapped during decompression shortly before

466          eruption (they were syn-eruptive) and are thus not representative of

467          pre-eruption storage conditions". For the many reasons discussed in

468          this paper, we disagree with this interpretation of inclusions in quartz

469          rims, and conclude instead that the temperatures derived by Gualda

470          and Ghiorso (2013a) for interior melt inclusions in samples of LBT

471          largely represent the same event, namely the pre-recharge

472          crystallization of quartz in EBT. Peppard et al. (2001) interpreted

473          their inclusion data as showing that "The near-rim, late erupted

474          (entrapped) inclusions have greater Zr (despite nearly similar $SiO_2$

475          wt%, see below), suggesting a higher temperature of entrapment

476          coeval with crystallization of CL bright-rim zones". The average Zr-

477          content of the seven high-Ba spots is 114 ppm, which would

478          correspond to about 758°C, and so it seems likely that none of the

479          analyzed MI truly represent LBT. Maximum Zr concentrations of 140

480          to 170 ppm were measured in Ba-enriched *matrix* glass of pumices

481          from Ig2 packages by Chamberlain et al. (2015), signifying

21

9/1/2015

482          temperatures in the range 775 to 792°C. We note here also that

483          Bindeman and Valley (2002) obtained zircon-saturation temperatures

484          of 760-800°C for the LBT and 730-735°C for the EBT (by measuring

485          bulk rock data, the mass of zircon crystallized, and the rock's crystal

486          content),     consistent     with     FeTi-oxide     and     oxygen-isotope

487          temperatures. A new calibration of zircon-saturation (Boehnke et al.

488          2013) suggests that the above zircon-saturation temperatures should

489          be lowered by 45-55°C for the Bishop Tuff Zr concentrations. We

490          conclude at this time that the zircon saturation temperatures for LBT

491          are higher than for EBT, but that the exact temperature values (down

492          to 675°C for 80 ppm Zr in EBT) may now be slightly too low.

493

494     **Melt Inclusions and reverse-zoned rims**

495

496          Elevated amounts of compatible trace elements such as Ti, Ba, Sr, and LREE,

497     and low concentrations of incompatible elements such as Rb and HREE that are

498     comparable to LBT whole-rock values were found only in a very small proportion of

499     quartz melt inclusions in LBT samples, and none in Early and Middle BT samples

500     (Wallace et al. 1999; Anderson et al. 2000). Melt inclusions in actual CL-bright rims

501     of quartz are evidently poorly represented in the analyzed population (Peppard et

502     al. 2001). This may in part be attributed to the fact that most MI in the bright rims

503     are devitrified, and the main goal of these studies was the volatiles rather than their

504     content of Ti, Ba, and Zr, etc.  Wallace et al. (1999) and Anderson et al. (2000) found

22

9/1/2015

505    the highest $CO_2$ contents of all (300 to more than 1000 ppm) in the MI in quartz *rims*

506    of LBT pumices, leading there to the highest gas saturation pressures (Wallace et al.

507    1999). With additional measurements, Roberge et al. (2013) suggested 150-200

508    MPa for early melt inclusions and 200-280 MPa for rim inclusions.

509          Many studies in the last two or three decades have raised legitimate

510    questions regarding how well the measured compositions of MI in magmatic

511    minerals faithfully retain the initial composition of the trapped liquid (e.g., Baker

512    2008). In the Bishop Tuff the more immediate question is whether, in their entirety,

513    MI in samples labelled EBT and LBT on stratigraphic grounds truly represent liquid

514    trapped from those different magmas, as assumed by Gualda et al. (2012a) and

515    Gualda and Ghiorso (2013a,b). Melt inclusions in LBT quartz, mostly in their dark

516    interiors, are highly evolved compositionally, very similar to EBT inclusions, and

517    very different from the average LBT composition (Gualda et al. 2012a). Some are

518    also partly faceted (Gualda et al. 2012b), probably a result of reheating, with the

519    potential for gain or loss of volatile constituents such as H and Li. In our opinion,

520    extensive and intensive parameters for the LBT event in the Bishop Tuff can only

521    safely be derived from melt inclusions clearly identified as occurring in the "bright

522    rims". Unfortunately, it seems that this is a very challenging task.

523          A key question is how fast these rims grew. Estimates range from a few days

524    (syn-eruptive growth, Gualda and Ghiorso, 2013a) to several centuries

525    (Chamberlain et al., 2014a). Some bright rims on quartz can measure up to 300

526    micrometers across (e.g. Wark et al. 2007), representing 20-30 % of the crystal

527    radii, and corresponding to 60 vol% of the crystals (Peppard  et al. 2001). Thus,

23

9/1/2015

528    following an initial dissolution step, there was in fact a considerable increment of

529    crystallization during the LBT event. Whereas rim growth during eruption would

530    proceed without needing nucleation, it would require very fast diffusion rates in the

531    liquid surrounding the crystals to feed such large rims. Based on modelling of Ti-in-

532    quartz    diffusion    timescales,    Chamberlain    et    al.    (2014a,    and    personal

533    communication) found that "at 760 °C, only 11 out of 151 profiles" would be

534    consistent with less than 10 years of diffusion following the LBT event. Profiles for

535    Ba and Sr in feldspar and Mg/Fe in pyroxene suggested longer time-scales as well

536    (Chamberlain et al. 2014a). The above observations indicate that decompression-

537    induced dissolution and growth during eruption is an unlikely explanation for the

538    CL-bright rims on LBT quartz.

539          Pamukcu et al. (2012) used the pattern of crystal-size distributions in LBT

540    quartz and feldspar to show that the fine-grained population (<100 micrometers)

541    crystallized    under    conditions    of    supersaturation    during    decompression.    This

542    population does not include "bright" overgrowths on pre-existing quartz and

543    sanidine phenocrysts. Elsewhere, granophyric textures have been shown to develop

544    by rapid growth following decompression in silicic ignimbrites (e.g. Lipman et al.

545    1997; Lowenstern et al. 1997). These microlitic and granophyric textures are logical

546    candidates    for    the    products    of    rapid,    syn-eruptive,    decompression-driven

547    crystallization, not the reversely-zoned rims that are seen on the Bishop Tuff

548    phenocrysts that significantly differ from EBT in their geochemistry. The "bright-

549    rim" event involved partial melting (clear resorption features, see for example

550    Peppard et al. 2001) followed by renewed crystallization of quartz and sanidine, a

24

9/1/2015

551     scenario more complex than decompression-driven crystallization. As stated by

552     Anderson et al. (2000, p. 460), "... both quartz and sanidine phenocrysts from the

553     late-erupted Bishop Tuff evidently grew from liquids that were increasingly Ba and

554     $CO_2$ rich.".

555

556     **Role of $CO_2$: elevated LBT temperatures**

557

558          Wallace et al. (1995, 1999), Anderson et al. (2001), and Roberge et al. (2013)

559     found 500-1000 ppm of $CO_2$ in LBT glass rim inclusions, in contrast to 6-300 ppm in

560     MI in early and middle-erupted pumices (see also summary plot in Ghiorso and

561     Gualda 2015). Their calculated values for $X_{H2O}$ of the attendant fluid compare well

562     with 0.59 obtained from VolatileCalc (Newman and Lowenstern 2002) for LBT

563     liquid at 820°C with 4 wt% $H_2O$ and 600 ppm $CO_2$ (Evans and Bachmann 2013).

564     Phase-equilibrium experiments on $H_2O$-$CO_2$-bearing magmas (including Holloway

565     and Burnham 1972; Rutherford et al. 1985) have shown that at fixed pressure and

566     temperature, increasing proportions of $CO_2$ in the fluid invariably increase magma

567     crystallinity and sometimes change phase assemblages. Although weakly soluble in

568     low pressure silicate melts, the addition of $CO_2$ to the fluid greatly diminishes the

569     $H_2O$-activity of the coexisting melt (Holloway 1976).

570          Data on the solubility of $H_2O$ and $CO_2$ in rhyolitic melts (Silver et al. 1990;

571     Blank et al. 1993; Zhang 1999; Tamic et al. 2001) may be used to extract values for

572     the fugacity of $CO_2$ and $H_2O$. This enables $CO_2$ to be expressed as a function of

573     temperature at fixed total pressure in terms of the mole fraction of $CO_2$ in a mixed

25

9/1/2015

574    $H_2O$-$CO_2$ fluid and wt% $H_2O$ in the melt (for example, Scaillet and Evans 1999, Table

575    2, their Fig. 12). Experimental solubility data show that the relationships between

576    $f$$CO_2$ and $CO_{2melt}$ (ppm) can be faithfully expressed as (see for instance Blank et al.

577    1993; Lesne et al. 2011):

578                    $$f CO_2 = aCO_{2(melt)}{}^b$$

579    where a and b are empirically fitted parameters specific to melt composition (see

580    Fig. 2 in Blank et al. 1993). By virtue of thermodynamic equilibrium between fluid

581    and melt, the relationships between $f$$CO_2$ and the mole fraction of $CO_2$ in the

582    coexisting fluid ($XCO_2$) are then given by the standard equation:

583                    $$f CO_2 = XCO_2 \, \gamma CO_2 {}^* \, P_{tot}$$

584    where $\gamma CO_2$ is the fugacity coefficient of $CO_2$ at the pressure and temperature of

585    interest, and $P_{tot}$ is the total pressure. The fugacity coefficient is determined using an

586    equation of state, in the present case the Modified Redlick-Kwong one (MRK,

587    Holloway 1987). For the sake of simplicity, we make the assumption that the fluid

588    follows the Lewis and Randall rule (ideal mixing of real fluids), which is equivalent

589    to saying that departure from ideality of any fluid species ($H_2O$ and $CO_2$) is not

590    affected by mixing, which is a good first approximation (see Ferry and Baumgartner

591    1987). Further assuming that the fluid is made primarily of $H_2O$ and $CO_2$ allows one

592    to find the corresponding $XH_2O$ (=1-$XCO_2$). We have used this procedure (Fig. 9) for

593    two granite compositions closely resembling EBT and LBT (Klimm et al. 2008),

594    whose phase diagrams are shown with added isopleths for $CO_2$ in the melt. At a

595    pressure of 200 MPa the presence of 600 ppm $CO_2$ in the melt and $X_{H2O}$ ⬚ 0.6 in the

26

9/1/2015

596    fluid elevates the solidus by about 75°C (from 665 to 740°C), and the quartz-

597    liquidus by about 90°C (from 675°C to 765°C).

598        The proximate cause of these increased temperatures is the sharply reduced

599    $H_2O$ activity. For 800 ppm $CO_2$ in the melt and and a corresponding $X_{H2O} \simeq 0.4$ in the

600    fluid, these temperatures rise by an additional 20-30°C. Several recent experimental

601    studies on granite compositions have been conducted in the presence of a binary

602    $H_2O$-$CO_2$ fluid. These consistently show increases in eutectic and liquidus

603    temperatures related to the lowered activity of $H_2O$ caused by the presence of $CO_2$ in

604    the system (Clemens and Wall 1981; Pichavant 1987; Keppler 1989; Ebadi and

605    Johannes 1991; Holtz et al. 1992; Scaillet et al. 1995; Dall'Agnol et al. 1999; Scaillet

606    and Evans 1999; Klimm et al. 2003; Bogaerts et al. 2006; Klimm et al. 2008).

607        While dissolved $CO_2$ in all cases is present in seemingly small quantities (a

608    few hundreds of ppm at most in silicic magmas), it does not imply that the magma

609    was especially $CO_2$-poor. Petrological and geochemical arguments have led to the

610    proposal that the Bishop Tuff magma was fluid-saturated prior to eruption (Wallace

611    et al. 1995; Wallace et al. 1999; Gualda and Anderson 2007), with amounts of fluid

612    ranging up to nearly 6 wt% (Wallace et al. 1995; Wallace et al. 1999). This, along

613    with the restored fluid compositions of Wallace et al (1999), implies that a non

614    trivial amount of $CO_2$ was present in the reservoir, even in the most water-rich end

615    member (EBT). For instance, for a magma containing 6 wt% fluid with a

616    composition of $XH_2O = 0.97$ (close to the highest $XH_2O$ inferred by Wallace et al.

617    1999), the bulk content of $CO_2$ is 0.4 wt%. For a magma with only 2 wt% exsolved

27

9/1/2015

618    fluid whose composition is $XH_2O=0.6$, the bulk $CO_2$ content of the magma increases

619    to 1.2 wt%.

620        Experiments on haplogranitic compositions (e.g., Holtz et al. 1992) showed

621    that the lower $H_2O$-activity caused by $CO_2$ in the fluid induces a shift in the ternary

622    minimum and eutectic compositions towards enrichment in Or relative to the Ab

623    component, and higher eutectic crystallization temperatures Whole-rock LBT is

624    similarly enriched in $K_2O/Na_2O$, that is, normative Or/Ab, compared to EBT

625    (Hildreth 1977). This provides further support for lower $H_2O$-activity in LBT caused

626    by $CO_2$ in the system and a higher temperature eutectic (Holtz et al. 1992). We

627    conclude that the presence of $CO_2$ in the LBT magma system is sufficient to account

628    for the elevated temperatures (780-820°C) extracted from magnetite-ilmenite

629    thermometry (cf. Ghiorso and Gualda 2013; Gualda and Ghiorso 2013a; Gardner et

630    al. 2014) in these least-evolved parts of the Bishop Tuff, notwithstanding their

631    content of quartz, sanidine, and plagioclase. The counter-argument for the minimal

632    influence of $CO_2$ developed by Gualda and Ghiorso (2013a, p. 769) was based on

633    their finding of similar zircon saturation temperatures for EBT and LBT, a result that

634    we consider untenable, as discussed above.

635        Despite a range in FeTi-oxide temperature from 700°C to ~780°C (Fig. 5),

636    evolved, high-$SiO_2$ EBT pumice shows only minimal compositional changes (in $TiO_2$,

637    FeO, CaO, Ba) that could be attributed to crystal fractionation. Although some

638    variability could be caused by post-eruption alteration, the whole-rock K/Na atomic

639    ratios of EBT are also a function of temperature (Fig.10). Again, this represents a

640    shift in the ternary minimum composition that could be related to a change in $H_2O$-

28

9/1/2015

641    activity. It is arguable, however, whether a change in the melt content of $CO_2$ (300

642    down to 6 ppm) is sufficient to drive this effect (Fig. 9). Certainly, the "eutectic"

643    assemblage Qz-San-Pl in such an evolved rhyolite composition as EBT is only

644    possible in the higher part of its temperature range if the activity of $H_2O$ is distinctly

645    less than one (see below, under IMPLICATIONS).

646

647    **Presence of pyroxenes**

648

649        We view it as no coincidence that the allegedly too-high FeTi-oxide

650    temperatures (> 770°C) tend to be from samples that contain two pyroxenes. These

651    are euhedral in outline, relatively homogeneous, and nearly uniform in intersample

652    composition (Hildreth and Wilson 2007). Except at the highest temperatures

653    (where we might call them phenocrysts), they are not in Fe/Mg-exchange

654    equilibrium with the FeTi-oxides, the biotite, or the inferred silicic liquid (Evans and

655    Bachmann 2013). We infer that the pyroxenes are a signal of hot conditions (e.g.,

656    824 ± 15°C from two-pyroxene thermometry, Frost and Lindsley 1992), that were

657    inherited from a recharge magma that existed prior to its mixing with slightly cooler

658    rhyolite above, an event that gave rise to the petrographic features that define LBT.

659    Experiments on rhyolite and dacite compositions (Fig. 9; Clemens and Wall 1981;

660    Dall'Agnol et al. 1999; Scaillet and Evans 1999; Klimm et al. 2003; Bogaerts et al.

661    2006; Klimm et al. 2008) have shown that the crystallization of orthopyroxene

662    requires relatively high temperature (generally >750°C) or undersaturation in $H_2O$,

663    or both. If the LBT magma was in fact stored on a millenium timescale at 730-750°C

29

9/1/2015

664    (Gualda et al. 2012b), we have to ask not only why euhedral orthopyroxene survived

665    but why, in a fluid-saturated $H_2O$-rich rhyolite magma, there are no signs of

666    corrosion of its crystal margins or growth of cummingtonite (or biotite?) at the

667    expense of orthopyroxene (± liquid) as, for example, in the Taupo rhyolites. It seems

668    highly unlikely that orthopyroxene could survive for millenia (way beyond

669    laboratory time scales) in an $H_2O$-rich vapor-saturated magma at T ≤ 740°C, which is

670    the scenario advocated by Gualda and Ghiorso (2013a) and Gardner et al. (2014).

671    Pyroxene was eliminated after one month in the experiments of Gardner et al.

672    (2014). The pyroxenes survived because they were injected into the highly silicic

673    melt pocket at the top of the Bishop Tuff reservoir only years to decades prior to

674    eruption.

675

676                    **PHASE EQUILIBRIUM EXPERIMENTS**

677

678        In petrological research on natural samples, we are seldom if ever in a

679    position to prove in any specific case that a state of equilibrium was reached and

680    frozen in. We use equilibrium criteria that are necessary but not sufficient, as in

681    element partitioning diagrams. We might agree, though, that the greater the number

682    of independent exchanges found to satisfy equilibrium criteria in any given case, the

683    more likely is equilibrium (which could be system wide, partial, or local, e.g.

684    Pichavant et al. 2007). Ultimately, laboratory reproduction of phase volumes and

685    compositions at known temperature, pressure, and volatile fugacities offers a

686    superior opportunity to resolve the question, but it is imperative that *all* intensive

30

9/1/2015

687    and extensive variables are a suitable match to the target of the investigation.

688    Ideally, simulated phase diagrams such as rhyolite-MELTS should be consistent with

689    corresponding experimental phase diagrams and mineral thermobarometry

690    (including those used in the calibration).

691         Early Bishop Tuff pumice is composed of high-silica rhyolite with sparse

692    phenocrysts of sodic plagioclase, as well as quartz, sanidine, biotite, magnetite, and

693    rare ilmenite. Many of the pumice samples are close in whole-rock composition to

694    haplogranite (Table 1). Their crystallization took place under vapor-saturated

695    conditions (Wallace et al. 1995, 1999). At 200 MPa, the water-saturated solidus of

696    haplogranite is 670°C (Pichavant 1987; Holtz et al. 1992; Scaillet et al. 1995;

697    Johannes and Holtz 1996). For an EBT Plinian pumice (which accommodates some

698    anorthite component), Scaillet and Hildreth (2001) found a water-saturated solidus

699    of 680°C at 200 MPa. Gualda and Ghiorso (2013b) computed crystallization

700    temperatures with rhyolite-MELTS for water-saturated EBT and LBT at 175 and 250

701    MPa and found almost identical eutectic crystallization temperatures for both (757-

702    760°C). Compared to the Scaillet and Hildreth (2001) experiments and others on

703    similar highly evolved natural granitic compositions (e.g. Klimm et al. 2003, 2008),

704    their simulations showed a water-saturated eutectic temperature for EBT that

705    seemed to at least 50°C too high. This reflected a problem with the entropy of the

706    liquid as modelled in rhyolite-MELTS, and a down-$T$ correction of 40°C is now

707    recommended (Gardner et al. 2014). The simulated temperatures for LBT, on the

708    other hand, did not account for the presence of $CO_2$ in the system. To

31

9/1/2015

709    counterbalance this omission, Gualda and Ghiorso (2013a, p. 763) suggested an up-

710    $T$ offset on the order of 20°C. In our opinion, this offset is inadequate.

711        Gardner et al. (2014) reported on hydrothermal laboratory experiments

712    designed to reproduce the crystallization conditions and mineralogy of a sample of

713    LBT rhyolite. The sample (AB-6202) was from the Ig2NWb sequence (Fig. 1), with a

714    crystallinity of 25.3 wt.% (Pamukcu et al. 2012). The sample was crushed to <100

715    μm (but not fused at high temperature) and held under $H_2O$-saturated conditions at

716    $T$ from 700 to 800°C and $P$ from 50 to 200 MPa for 4.8 to 25.9 days, with redox

717    conditions inferred to be around NNO imposed on the sample by the vessel. Gardner

718    et al. (2014, p. 9) found that orthopyroxene, almost a signature mineral for LBT, was

719    "not stable experimentally" under any of the hydrous conditions used, and they

720    concluded that LBT magma was stored at ≤740°C.

721        Three experiments at 785°C and 200-250 MPa (Gardner et al. 2014) were

722    conducted under mixed volatile conditions ($H_2O$ + $CO_2$). The run with most $CO_2$

723    (701±52 ppm in product glass, and 3.91±0.23 wt% $H_2O$) yielded orthopyroxene,

724    sanidine, and oxide; the sanidine and oxide (magnetite?) both occur 65°C higher

725    than their respective liquidus curves under $H_2O$-saturated conditions at 200 MPa

726    (Gardner et al. 2014). These results are in general agreement with those of Klimm et

727    al. (2008) which showed that orthopyroxene is stable at $H_2O_{melt}$ < 4.5 wt% (Fig. 9).

728    Nevertheless, Gardner et al. (2014) concluded that "at constant total pressure, the

729    addition of trace amounts of $CO_2$ to the melt phase would have little noticeable effect

730    on the phase diagram". This conclusion seems to ignore the fact that, at the

32

9/1/2015

731    pressures considered, 700 ppm $CO_2$ in the melt will be sustained by a mixed volatile

732    fluid with $X_{CO2}$ and $X_{H2O}$ around 0.5 (Fig. 9).

733        We interpret phase-equilibrium experiments to tell us that at 200 MPa

734    eutectic temperatures in the vicinity of 700°C are to be expected for evolved

735    granitic, $CO_2$-free, $H_2O$-saturated compositions like those of the EBT, whereas

736    eutectic temperatures of ~800°C will be the case for less evolved magmas like LBT

737    containing 600-1000 ppm of $CO_2$ in the liquid (corresponding however to

738    significantly larger bulk $CO_2$ contents, on the order of 1 wt%, as explained above), in

739    equilibrium with orthopyroxene (Fig. 9). EBT eutectic temperatures higher than

740    700°C could be attributed to small amounts (6-300 ppm) of $CO_2$ in the liquid, or to a

741    process of partial melting in a  but ma mush zone underlying mainly liquid EBT (see

742    below under IMPLICATIONS). These temperatures mimic rather well those

743    indicated by FeTi-oxide and two-feldspar thermometry from the main suite of the

744    BishopTuff, a very satisfying result from the viewpoint of equilibrium.

745

746                                    **MAGMA MIXING**

747

748        Evidence from the literature for magma recharge followed by magma mixing

749    in the Bishop Tuff was reviewed in some detail by Evans and Bachmann (2013). The

750    process has been found to be commonplace in upper crustal magma reservoirs. It

751    has been invoked by a lengthy list of investigators for the Bishop Tuff and several

752    other volcanic centers, some similar petrologically to the Bishop Tuff (e.g., Bandelier

753    Tuff, Goff et al. 2014; Wolff and Ramos 2014). The process of magma mixing

33

9/1/2015

754    (recharge) is inherent to incrementally-growing upper crustal magma reservoirs, as

755    advocated by numerous authors in recent years (e.g., Lipman 2007; Annen 2009;

756    Miller et al. 2011; Gelman et al. 2013; Laumonier et al. 2014).

757        In the Bishop Tuff, the petrographic evidence for magma mixing is far from

758    hidden. In the late Bishop Tuff, we see two pyroxenes that equilibrated basically

759    with a single magma composition (constant Mg-number), in association with FeTi-

760    oxides and biotite that crystallized from magma showing *evolving* compositions

761    (Evans and Bachmann 2013), together with partially resorbed quartz and sanidine,

762    both of which underwent marginal growth and element enrichment due to contact

763    at a late stage with less evolved, hotter $CO_2$-bearing magma. Recognition of this

764    recharge event is a prerequisite for avoiding missteps in the interpretation of many

765    of the petrologic details in the Bishop Tuff, for example the melt inclusions.

766        Except for $K_2O$ and $Na_2O$, the measured contents of major elements in the

767    melt inclusions of EBT and LBT samples are practically identical (Gualda et al.

768    2012a). As noted by Wallace et al. (1999), melt inclusions in EBT are almost

769    identical in composition to whole-rock EBT, whereas in LBT there are significant

770    differences in $SiO_2$, $TiO_2$, FeO, MgO, and CaO between WR and inclusions. These

771    differences could be related to the greater proportion of crystals in typical LBT, but,

772    given that ⊡95 % of crystals are feldspar (predominantly sanidine) and quartz

773    (Hildreth and Wilson 2007), this explanation does not explain the differences in FeO

774    and MgO.

775        EBT is highly evolved silica-rich rhyolite (average $SiO_2$ = 77.6 wt%), with

776    only very small variations in most major and trace elements (Fig. 5). We plot $K_2O$

34

9/1/2015

777     and $Na_2O$ (Fig. 10) with some reluctance, knowing the tendency for these

778     constituents to undergo post-eruption alteration, typically with loss of Na (Hildreth

779     and Wilson 2007). Nevertheless, whole-rock K/Na for EBT samples increases up-

780     temperature from 0.81 to 0.95 (Fig. 10). K/Na atomic ratios of MI average 0.81 in

781     EBT and range from 0.83 to 1.07 in LBT (the latter based provisionally on samples

782     with > 80 ppm Ba). There is thus a trend in the MI analyses for K/Na to be higher in

783     the less evolved, higher FeTi-temperature (and higher zircon temperature) magma.

784     This trend mirrors the one seen in the whole-rock compositions. The comparison

785     suggests that recharge LBT magma engulfed deep, "hot" rather than average (⬚

786     730°C) or low-temperature (⬚ 700°C) EBT magma. The growth of "bright rims"

787     around the dark interiors of quartz and sanidine antecrysts that characterize LBT

788     pumice tells us that *only* rim MI will give us the composition of LBT magma at the

789     time (e.g., Roberge et al. 2013). By including all the MI in quartz, Gualda and Ghiorso

790     (2013a, b) found identical values of intensive parameters for EBT and LBT. Because

791     the MI in CL-bright rims of quartz are few, small, decrepitated (Pamukcu et al.

792     2012), or hard to find, they have not been adequately sampled for their major or

793     minor elements. When petrogenetic studies do not recognize these limitations

794     (Ghiorso and Gualda 2013; Gualda and Ghiorso 2013a; Gualda and Ghiorso 2013b),

795     conclusions then conflict with FeTi-oxide and other thermometers that are

796     supported by kinetics sufficiently fast to register late events in the magma sequence.

797         The mixing process resulted in matrix glass compositions in LBT *less* evolved

798     than glass inclusions (Roberge et al. 2013), which is the inverse of simple, one-stage

799     crystallization. According to Roberge et al. (2013): "the cores of quartz phenocrysts

35

9/1/2015

800    in LBT largely crystallized from more evolved melts at an earlier stage (EBT), and

801    then were later incorporated into less evolved rhyolite melts from the underlying

802    crystal mush zone". In addition, Chamberlain et al. (2014b) showed that CL bright

803    rims of zircon in LBT have measurably smaller contents than dark interiors of

804    incompatible elements such as U and HREE.

805          With a relatively late magma mixing event such as the one recorded in the

806    Bishop Tuff, the petrologist sees parts of the system that accommodated and appear

807    to have reached equilibrium (FeTi-oxides, biotite, plagioclase and liquid), and other

808    parts that either largely failed (pyroxenes) or only partially maintained equilibrium

809    with the melt (quartz and sanidine). When we view whole-rock compositions of

810    LBT, we must remember that these do not represent something that was ever 100 %

811    liquid. Whole-rock compositions could have been enriched in K (by sanidine), Si (by

812    quartz), or Mg and Fe (pyroxenes). Their crystal content (12-25 wt.%, Hildreth and

813    Wilson 2007, Table 1) thus includes the products of in-situ crystallization

814    (plagioclase, biotite, and oxides) as well as inherited crystals from the recharge

815    (pyroxenes).

816          We prefer the hypothesis of partial melting of a cumulate mush (Deering et

817    al. 2011; Bachmann et al. 2014; Wolff et al. in press) to explain the compositional

818    variations in minor elements in EBT (Fig. 5). By the melting of anhydrous solids, this

819    process depletes the content of $H_2O$ in the liquid and thus maintains the eutectic

820    nature of the mineral assemblage, with only small changes in major element

821    contents (Wolff et al. in press) but significant variations in trace elements, including

822    the striking LREE enrichment with FeTi-oxide temperatures.

36

9/1/2015

823

824                                    **IMPLICATIONS**

825

826           The temperature span of slightly more than 100°C indicated by FeTi-oxide

827    thermometry  for  the  Bishop  Tuff  encompasses  attendant  crystal-liquid

828    fractionation and mixing in a shallow sub-volcanic magma reservoir influenced by a

829    late-stage magma recharge event (leading to the mixed LBT) coming from below.

830    The negative assessment of FeTi-oxide thermometry in the Bishop Tuff by Ghiorso

831    and Gualda (2013) is flawed because if fails to recognize the range of $TiO_2$ contents

832    of the magma in the Bishop Tuff induced by fractionation/recharge. The positive

833    slope of *$aTiO_2$* vs. temperature is not an indication of disequilibrium in the FeTi-

834    oxides.  Smooth  correlations  between  FeTi-oxide  thermometry  and  pumice  and

835    mineral compositions make it very unlikely the temperatures are seriously in error.

836    The  presence  of  600-1000  ppm  $CO_2$  in  quartz-rim  melt  inclusions  and  the

837    corresponding  lower  *$aH_2O$*  enable  us  to  reconcile  published  phase-equilibrium

838    experiments with the ⬚800°C oxide temperatures. Calculated mole fractions of $H_2O$

839    in the LBT fluid are 0.6 or smaller, elevating eutectic and solidus temperatures by as

840    much as 80-100°C.

841           On the basis of petrographic and geochemical observations accumulated over

842    the last four decades, we favor a model that involves late-stage magma mixing and

843    cumulate  remobilization  at  the  base  of  a  crystal-poor  high-SiO2  rhyolite  cap

844    extracted from a long-lived sub-volcanic silicic mush (see Hildreth, 2004 for a

845    cartoon). This model permits a coherent understanding of the spatial, temporal,

37

9/1/2015

846    microstructural, geochemical, and mineralogical features of the erupted products.

847    These allow us to make sense of the complete $logfO_2$-$T$ record of magma chamber

848    conditions provided by the FeTi-oxides. Remarkable as it may seem to some, it

849    would appear that among the mineral thermometers that have been applied to the

850    Bishop Tuff, the ilmenite-magnetite thermometer remains virtually unmatched in its

851    precision, accuracy, and inclusive coverage of magma chamber evolution.

852

859                              **REFERENCES CITED**


860

861    Anderson, A.T., Davis, A.M., and Lu, F. (2000) Evolution of Bishop Tuff rhyolitic

862         magma based on melt and magnetite inclusions and zoned phenocrysts.

863         Journal of Petrology, 41(3), 449-473.

864    Annen, C. (2009) From plutons to magma chambers: Thermal constraints on the

865         accumulation of eruptible silicic magma in the upper crust. Earth and

866         Planetary Science Letters, 284(3-4), 409-416.

38

9/1/2015

867    Bachmann, O., Deering, C., Lipman, P., and Plummer, C. (2014) Building zoned

868          ignimbrites by recycling silicic cumulates: insight from the 1,000 km$^3$

869          Carpenter Ridge Tuff, CO. Contributions to Mineralogy and Petrology, 167(6),

870          1-13.

871    Bacon, C.R., and Hirschmann, M.M. (1988) Mg/Mn partitioning as a test for

872          equilibrium between coexisting Fe-Ti oxides. American Mineralogist, 73, 57-

873          61.

874    Baker, D.R. (2008) The fidelity of melt inclusions as records of melt composition.

875          Contributions to Mineralogy and Petrology, 156(3), 377-395.

876    Bindeman, I.N., and Valley, J.W. (2002) Oxygen isotope study of the Long Valley

877          magma system, California: isotope thermometry and convection in large

878          silicic magma bodies. Contributions to Mineralogy and Petrology, 144, 185-

879          205.

880    Blank, J.G., Stolper, E.M., and Carroll, M.R. (1993) Solubilities of carbon dioxide and

881          water in rhyolitic melt at 850 ºC and 750 bars. Earth and Planetary Science

882          Letters, 119(1-2), 27-36.

883    Blundy, J., and Cashman, K. (2008) Petrologic Reconstruction of Magmatic System

884          Variables and Processes. Reviews in Mineralogy and Geochemistry, 69(1),

885          179-239.

886    Boehnke, P., Watson, E.B., Trail, D., Harrison, T.M., and Schmitt, A.K. (2013) Zircon

887          saturation re-revisited. Chemical Geology, 351(0), 324-334.

9/1/2015

888    Bogaerts, M., Scaillet, B., and Auwera, J.V. (2006) Phase Equilibria of the Lyngdal

889        Granodiorite (Norway): Implications for the origin of metaluminous ferroan

890        granitoids. J. Petrology, 47(12), 2405-2431.

891    Chamberlain, K.J., Morgan, D.J., and Wilson, C.J.N. (2014a) Timescales of mixing and

892        mobilisation in the Bishop Tuff magma body: perspectives from diffusion

893        chronometry. Contributions to Mineralogy and Petrology, 168(1), 1-24.

894    Chamberlain, K.J., Wilson, C.J.N., Wooden, J.L., Charlier, B.L.A., and Ireland, T.R.

895        (2014b) New Perspectives on the Bishop Tuff from Zircon Textures, Ages and

896        Trace Elements. Journal of Petrology, 55(2), 395-426.

897    Chamberlain, K.J., Wilson, C.J.N., Wallace, P.J., and Millet, M.-A. (2015) Micro-

898        analytical Perspectives on the Bishop Tuff and its Magma Chamber. Journal of

899        Petrology, 56(3), 605-640.

900    Clemens, J., and Wall, V.J. (1981) Origin and crystallization of some peraluminous (S-

901        type) granitic magmas. Canadian Mineralogist, 79, 111-131.

902    Dall'Agnol, R., Scaillet, B., and Pichavant, M. (1999) An Experimental Study of a

903        Lower Proterozoic A-type Granite from the Eastern Amazonian Craton,

904        Brazil. Journal of Petrology, 40(11), 1673-1698.

905    Deering, C.D., Bachmann, O., and Vogel, T.A. (2011) The Ammonia Tanks Tuff:

906        Erupting a melt-rich rhyolite cap and its remobilized crystal cumulate. Earth

907        and Planetary Science Letters, 310(3-4), 518-525.

908    Ebadi, A., and Johannes, W. (1991) Beginning of melting and composition of first

909        melts in the system $Qz$-$Ab$-$Or$-$H_2O$-$CO_2$. Contributions to Mineralogy and

910        Petrology, 106(3), 286-295.

40

9/1/2015

911     Evans, B.W., and Bachmann, O. (2013) Implications of equilibrium and

912          disequilibrium among crystal phases in the Bishop Tuff. American

913          Mineralogist, 98, 271-274.

914     Ferry, J.M., and Baumgartner, L. (1987) Thermodynamic models of molecular fluids

915          at the elevated pressures and temperatures of crustal metamorphism.

916          Reviews in Mineralogy and Geochemistry, 17(1), 323-365.

917     Frost, B.R., and Lindsley, D.H. (1991) Occurrence of iron-titanium oxides in igneous

918          rocks. In Ribbe, Ed, 25, p. 433-468. Mineralogical Society of America.

919     Frost, B.R., and Lindsley, D.H. (1992) Equilibria among Fe-Ti oxides, pyroxenes,

920          olivine, quartz. Part II, Application. American Mineralogist, 77, 1004-1020.

921     Gardner, J., Befus, K., Gualda, G.A.R., and Ghiorso, M. (2014) Experimental

922          constraints on rhyolite-MELTS and the Late Bishop Tuff magma body.

923          Contributions to Mineralogy and Petrology, 168(2), 1-14.

924     Gelman, S.E., Gutierrez, F.J., and Bachmann, O. (2013) The longevity of large upper

925          crustal silicic magma reservoirs. Geology, 41, 759-762.

926     Ghiorso, M.S., and Sack, R.O. (1991) Fe-Ti oxide geothermometry: thermodynamic

927          formulation and the estimation of intensive variables in silicic magmas.

928          Contributions to Mineralogy and Petrology, 108, 485-510.

929     Ghiorso, M.S., and Evans, B.W. (2008) Thermodynamics of rhombohedral oxide solid

930          solutions and a revision of the Fe-Ti oxide geothermometer and oxygen-

931          barometer. American Journal of science, 308(9), 957-1039.

932     Ghiorso, M.S., and Gualda, G.A.R. (2013) A method for estimating the activity of

933          titania in magmatic liquids from the compositions of coexisting

41

9/1/2015

934        rhombohedral and cubic iron-titanium oxides. Contributions to Mineralogy

935        and Petrology, 165(1), 73-81.

936   Ghiorso, M., and Gualda, G.A.R. (2015) An $H_2O$-$CO_2$ mixed fluid saturation model

937        compatible with rhyolite-MELTS. Contributions to Mineralogy and Petrology,

938        169(6), 1-30.

939   Goff, F., Warren, R.G., Goff, C.J., and Dunbar, N. (2014) Eruption of reverse-zoned

940        upper Tshirege Member, Bandelier Tuff from centralized vents within Valles

941        caldera, New Mexico. Journal of Volcanology and Geothermal Research,

942        276(0), 82-104.

943   Gualda, G.R., and Anderson, A., Jr. (2007) Magnetite scavenging and the buoyancy of

944        bubbles in magmas. Part 1: Discovery of a pre-eruptive bubble in Bishop

945        rhyolite. Contributions to Mineralogy and Petrology, 153(6), 733-742.

946   Gualda, G.A.R., Ghiorso, M.S., Lemons, R.V., and Carley, T.L. (2012a) Rhyolite-MELTS:

947        A modified calibration of MELTS optimized for silica-rich, fluid-bearing

948        magmatic systems. Journal of Petrology, 53(5), 875-890.

949   Gualda, G.A.R., Pamukcu, A.S., Ghiorso, M.S., Anderson, A.T., Jr., Sutton, S.R., and

950        Rivers, M.L. (2012b) Timescales of Quartz Crystallization and the Longevity

951        of the Bishop Giant Magma Body. PLoS ONE, 7(5), e37492.

952   Gualda, G.A.R., and Ghiorso, M.S. (2013a) The Bishop Tuff giant magma body: an

953        alternative to the Standard Model. Contributions to Mineralogy and

954        Petrology, 166(3), 755-775.

955   Gualda, G.A.R., and Ghiorso, M.S. (2013b) Low-pressure origin of high-silica rhyolites

956        and granites. The Journal of Geology, 121(5), 537-545.

42

9/1/2015

957    Hervig, R.L., and Dunbar, N.W. (1992) Cause of chemical zoning in the Bishop
958        (California) and Bandelier (New Mexico) magma chambers. Earth and
959        Planetary Science Letters, 111, 97-108.

960    Hildreth, W. (1977) The magma chamber of the BishopTuff: gradients in
961        temperature, pressure, and composition. Ph.D thesis, University of California,
962        Berkeley.

963    Hildreth, W. (1979) The Bishop Tuff: evidence for the origin of the compositional
964        zonation in silicic magma chambers. In C.E. Chapin, and W.E. Elston, Eds. Ash-
965        Flow Tuffs, 180, p. 43-76. Geological Society of America, Special Paper 180.

966    Hildreth, W. (1981) Gradients in silicic magma chambers: Implications for
967        lithospheric magmatism. Journal of geophysical research, 86(B11), 10153-
968        10192.

969    Hildreth, W.S., and Wilson, C.J.N. (2007) Compositional Zoning in the Bishop Tuff.
970        Journal of Petrology, 48(5), 951-999.

971    Holloway, J.R. (1976) Fluids in the evolution of granitic magmas: Consequences of
972        finite $CO_2$ solubility. Geological Society of America Bulletin, 87(10), 1513-
973        1518.

974    Holloway, J.R. (1987) Igneous fluids. Reviews in Mineralogy and Geochemistry, 17,
975        211-233.

976    Holloway, J.R., and Burnham, C.W. (1972) Melting relations of basalt with
977        equilibrium water pressure less than total pressure. Journal of Petrology,
978        13(1), 1-29.

43

9/1/2015

979    Holtz, F., Pichavant, M., Barbey, P., and Johannes, W. (1992) Effects of $H_2O$ on

980        liquidus phase relations in the haplogranite system at 2 and 5 kbar. American

981        Mineralogist 77, 1223-1241.

982    Johannes, W., and Holtz, F. (1996) Petrogenesis and experimental petrology of

983        granitic rocks. 335 p. Springer-Verlag, Berlin.

984    Keppler, H. (1989) The influence of the fluid phase composition on the solidus

985        temperatures in the haplogranite system $NaAlSi_3O_8$-$KAlSi_3O_8$-$SiO_2$-$H_2O$-$CO_2$.

986        Contributions to Mineralogy and Petrology, 102(3), 321-327.

987    Klimm, K., Holtz, F., Johannes, W., and King, P.L. (2003) Fractionation of

988        metaluminous A-type granites: an experimental study of the Wangrah Suite,

989        Lachlan Fold Belt, Australia. Precambrian Research, 124(2-4), 327-341.

990    Klimm, K., Holtz, F., and King, P.L. (2008) Fractionation vs. magma mixing in the

991        Wangrah Suite A-type granites, Lachlan Fold Belt, Australia: Experimental

992        constraints. Lithos, 102(3-4), 415-434.

993    Laumonier, M., Scaillet, B., Pichavant, M., Champallier, R., Andujar, J. and Arbaret, L.

994        (2014) On the conditions of magma mixing and its bearing on andesite

995        production in the crust. Nature communications, 5.

996    Lesne, P., Scaillet, B., Pichavant, M., and Beny, J.-M. (2011) The carbon dioxide

997        solubility in alkali basalts: an experimental study. Contributions to

998        Mineralogy and Petrology, 162(1), 153-168.

999    Lindsley, D.H., Frost, B.R., Ghiorso, M.S., and Sack, R.O. (1991) Oxides Lie: The Bishop

1000       Tuff did not erupt from a thermally zoned magma body. EOS Transaction,

1001       American Geophysical Union, 72(17), 313.

44

9/1/2015

1002   Lipman, P.W. (2007) Incremental assembly and prolonged consolidation of

1003         Cordilleran magma chambers: Evidence from the Southern Rocky Mountain

1004         Volcanic Field. Geosphere, 3(1), 1-29.

1005   Lipman, P.W., Dungan, M.A., and Bachmann, O. (1997) Comagmatic granophyric

1006         granite in the Fish Canyon Tuff, Colorado: Implications for magma-chamber

1007         processes during a large ash-flow eruption. Geology, 25(10), 915-918.

1008   Lowenstern, J.B., Clynne, M.A., and Bullen, T.D. (1997) Co-magmatic A-type

1009         granophyre and rhyolite from the Alid volcanic center, Eritrea, Northwest

1010         Africa. Journal of Petrology, 38(12), 1707-1721.

1011   Miller, C.F., Furbish, D.J., Walker, B.A., Claiborne, L.L., Koteas, G.C., Bleick, H.A., and

1012         Miller, J.S. (2011) Growth of plutons by incremental emplacement of sheets

1013         in crystal-rich host: Evidence from Miocene intrusions of the Colorado River

1014         region, Nevada, USA. Tectonophysics, 500(1-4), 65-77.

1015   Newman, S., and Lowenstern, J.B. (2002) VolatileCalc: a silicate melt-$H_2O$-$CO_2$

1016         solution model written in Visual Basic for excel. Computers & Geosciences,

1017         28(5), 597-604.

1018   Pamukcu, A.S., Gualda, G.A.R., and Anderson, A.T. (2012) Crystallization Stages of the

1019         Bishop Tuff Magma Body Recorded in Crystal Textures in Pumice Clasts.

1020         Journal of Petrology, 53(3), 589-609.

1021   Peppard, B.T., Steele, I.M., Davis, A.M., Wallace, P.J., and Anderson, A.T. (2001) Zoned

1022         quartz phenocrysts from the rhyolitic Bishop Tuff. American MIneralogist,

1023         86, 1034-1052.

45

9/1/2015

1024  Pichavant, M. (1987) Effects of B and $H_2O$ on liquidus phase relations in the

1025     haplogranite system at 1 kbar. American Mineralogist, 72, 1056-1070.

1026  Pichavant, M., Costa, F., Burgisser, A., Scaillet, B., Martel, C. and Poussineau, S. (2007)

1027     Equilibrium scales in silicic to intermediate magmas: implications for

1028     experimental studies. Journal of Petrology, egm045.

1029  Roberge, J., Wallace, P.J., and Kent, A.J.R. (2013) Magmatic processes in the Bishop

1030     Tuff rhyolitic magma based on trace elements in melt inclusions and pumice

1031     matrix glass. Contributions to Mineralogy and Petrology, 165(2), 237-257.

1032  Rutherford, M.J., Sigurdsson, H., Carey, S., and Davis, A.M. (1985) The May 18, 1980,

1033     eruption of Mount St. Helens, 1. Melt composition and experimental phase

1034     equilibria. Journal of Geophysical Research, 90, 2929-2947.

1035  Scaillet, B., and Evans, B.W. (1999) The 15 June 1991 eruption of Mount Pinatubo. I.

1036     Phase equilibria and pre-eruption P-$T$-$f$O$_2$-$f$H$_2$O conditions of the dacite

1037     magma. Journal of Petrology, 40(3), 381-411.

1038  Scaillet, B., and Hildreth, W. (2001) Experimental constraints on the origin and

1039     evolution of the Bishop Tuff. In K. Knesel, G.B. Bergantz, and J. Davidson, Eds.

1040     Penrose Conference: Longevity and Dynamics of Rhyolitic Magma Systems.

1041     Geological Society of America.

1042  Scaillet, B., Pichavant, M., and Roux, J. (1995) Experimental crystallization of

1043     leucogranite magmas. Journal of Petrology, 36, 663-705.

1044  Silver, L., Ihinger, P., and Stolper, E. (1990) The influence of bulk composition on the

1045     speciation of water in silicate glasses. Contributions to Mineralogy and

1046     Petrology, 104(2), 142-162.

46

9/1/2015

1047    Tamic, N., Behrens, H. and Holtz, F. (2001) The solubility of $H_2O$ and $CO_2$ in rhyolite

1048        melts in equilibrium with a mixed $CO_2$-$H_2O$ fluid phase. Chemical Geology,

1049        174, 333-347.

1050    Thomas, J.B., and Watson, E.B. (2012) Application of the Ti-in-quartz

1051        thermobarometer to rutile-free systems. Reply to: a comment on: "TitaniQ

1052        under pressure: the effect of pressure and temperature on the solubility of Ti

1053        in quartz" by Thomas et al. Contributions to Mineralogy and Petrology,

1054        164(2), 369-374.

1055    Thomas, J.B., Watson, E.B., Spear, F.S. and Wark, D.A. (2015) TitaniQ recrystallized:

1056        experimental confirmation of the original Ti-in-quartz calibrations.

1057        Contributions to Mineralogy and Petrology, 169, 27-43.

1058    Wallace, P.J., Anderson, A.T., and Davis, A.M. (1995) Quantification of pre-eruptive

1059        exsolved gas contents in silicic magmas. Nature, 377, 612-615.

1060    Wallace, P.J., Anderson, A.T., and Davis, A.M. (1999) Gradients in $H_2O$, $CO_2$, and

1061        exsolved gas in a large-volume silicic magma chamber: interpreting the

1062        record preserved in the melt inclusions from the Bishop Tuff. Journal of

1063        Geophysical Research, 104(B9), 20097-20122.

1064    Wark, D.A., Hildreth, W., Spear, F.S., Cherniak, D.J., and Watson, E.B. (2007) Pre-

1065        eruption recharge of the Bishop magma system. Geology, 35(3), 235-238.

1066    Watson, E.B., and Harrison, T.M. (1983) Zircon saturation revisited: temperature

1067        and composition effects in a variety of crustal magma types. Earth and

1068        Planetary Science Letters, 64, 295–304.

47

9/1/2015

Wilson, C.J.N., Blake, S., Charlier, B.L. and Sutton, A.N. (2006) The 26.5 ka Oruani eruption, Taupo volcano, New Zealand: development, characteristics and evacuation of a large rhyolitic magma body. Journal of Petrology, 47, 35-69.

Wolff, J.A., and Ramos, F.C. (2014) Processes in Caldera-Forming High-Silica Rhyolite Magma: Rb,ÄìSr and Pb Isotope Systematics of the Otowi Member of the Bandelier Tuff, Valles Caldera, New Mexico, USA. Journal of Petrology, 55(2), 345-375.

Wolff, J.A., Ellis, B.S., Ramos, F.C., Starkel, W.A., Boroughs, S., Olin, P.H., and Bachmann, O. (in press) Remelting of cumulates as a process for producing chemical zoning in silicic tuffs: a comparison of cool, wet and hot, dry rhyolitic magma systems. Lithos, XXXX.

Zhang, Y. (1999) $H_2O$ in rhyolitic glasses and melts: Measurement, speciation, solubility, and diffusion. Reviews of Geophysics, 37(4), 493-516.

**FIGURE CAPTIONS**

Figure 1: (a) Simpified map and packages of deposits in the Bishop Tuff. The SW cluster of glaciated remnants includes superimposed packages of both Ig1SW and Ig2SW. (b) pumice clast proportions of the different Bishop Tuff emplacement units. Diagonal lines indicate ranges in deposits. The succession of emplacement units (Ig, ignimbrite package; F fall unit) is detailed in Hildreth and Wilson (2007). Modified from Hildreth and Wilson (2007).

48

9/1/2015

1092

1093    Figure 2: Ba (ppm) vs. $TiO_2$ (wt.%) in Bishop Tuff pumice (whole-rock) excluding 4

1094    trachydacites and 2 dark pumices, from Hildreth and Wilson (2007, Appendix 4), and

1095    melt inclusions, from Wallace et al. (1999), Anderson et al. (2000), and Peppard et al.

1096    (2001). Note the similar trends but contrasting ranges in the two populations. Melt

1097    inclusion data are predominantly from CL-dark quartz interiors.

1098

1099    Figure 3. Frequency histograms for $X_{Mg}$ (= atomic $Mg/(Mg+Fe^{2+})$ in ilmenite and

1100    magnetite in the Bishop Tuff. Data from Hildreth (1977) and Hildreth and Wilson (2007,

1101    Appendix 3). This updates histograms in Gualda and Ghiorso (2013a) and Gardner at al.

1102    (2014). Data from sample BT129 were omitted because the ilmenite contains 14%

1103    pyrophanite component, anomalously little Mg ($X_{Mg}$ =0.01), and is clearly out of MgFe-

1104    exchange equilibrium with its coexisting magnetite (Evans and Bachmann (2013). It was

1105    probably vapor-phase modified (Hildreth and Wilson 2007).

1106

1107    Figure 4. Frequency histogram for whole-rock Ba and Sr concentrations in main suite of

1108    the Bishop Tuff pumice. From dataset of Hildreth and Wilson (2007, Appendix 4).

1109

1110    Figure 5. Correlation between FeTi-oxide temperature and whole-rock compositions for

1111    four compatible elements (a, c, e, f) and two incompatible elements (b, d) in the main

1112    array of the Bishop Tuff. Outlier samples B355B and B383B (stars) are inferred to have

1113    undergone post-depositional changes (Evans and Bachmann, 2013). Seven duplicate

49

9/1/2015

1114    oxide pairs were averaged. Data taken from Hildreth (1977) and Hildreth and Wilson

1115    (2007, Appendices 3 and 4) and Ghiorso and Evans (2008).

1116

1117    Figure 6. Weight ratio Mn/Mg and atomic ratio $Mg/(Mg+Fe^{2+})$ of magnetite and ilmenite

1118    versus FeTi-oxide temperature for all analyzed pairs in the Bishop Tuff. Data from

1119    Hildreth (1977), Hildreth and Wilson (2007) and Ghiorso and Evans (2008).

1120

1121    Figure 7: Curve of $aTiO_2$ vs. $T$ at 200 MPa for a Bishop Tuff composition with 0.08 wt%

1122    $TiO_2$ and corresponding loci of the Fe-Ti oxides (dots), from Ghiorso and Gualda (2013),

1123    compared to the expected change in $aTiO2$ vs. $T$ (dashed line) assuming a difference of

1124    X2.5 in melt $TiO_2$ between EBT at 700°C and LBT at 800°C (see text for details).

1125

1126    Figure 8: $TiO_2$ content vs. $T$ for high-silica matrix melts saturated in FeTi oxides in high-

1127    temperature experiments on three fused granitoids (Klimm et al. 2003; Klimm et al.

1128    2008), showing the igneous compatibility of $TiO_2$ at $fO2 < \sim$ NNO (decrease of $TiO_2$ as a

1129    function of $T$).

1130

1131    Figure 9. Experimental results for crystallization at 200 MPa of two fused

1132    leucogranites AB421 and AB401 (as proxies for average LBT and EBT rhyolites, see

1133    Table 1; from Klimm et al. 2008; temperatures determined by thermocouples),

1134    contoured for ppm $CO_2$ in the melt.

1135

50

9/1/2015

1136    Figure 10.  Diagram showing that WR samples of hot (LBT and EBT) Bishop Tuff

1137    pumice have higher atomic K/Na than cooler (⬚700°C) EBT samples. Some of the

1138    higher K/Na samples may have been altered by post-eruption hydration (see text).

1139    Stars: see Fig. 5 caption. Data from Hildreth and Wilson (2007).

1140

1141

1142

1143

1144

1145

1146

1147

9/1/2015

1148  **TABLES**

1149

1150  Table 1. Comparison of the compositions of granite experimental charges with averages

1151  of early and late and pyroxene-bearing the Bishop Tuff

1152

| | AB421 | LBT | PX-LBT | AB401 | EBT |
|---|---|---|---|---|---|
| wt.% | | | | | |
| $SiO_2$ | 75.32 | 75.5 | 75.19 | 76.67 | 77.4 |
| $TiO_2$ | 0.15 | 0.21 | 0.19 | 0.09 | 0.07 |
| $Al_2O_3$ | 12.71 | 13.0 | 13.36 | 12.10 | 12.3 |
| FeO | 1.62 | 1.1 | 1.23 | 0.92 | 0.7 |
| MnO | 0.06 | 0.03 | 0.03 | 0.02 | 0.04 |
| MgO | 0.23 | 0.25 | 0.27 | 0.05 | 0.01 |
| CaO | 0.90 | 0.95 | 0.94 | 0.53 | 0.45 |
| $Na_2O$ | 3.36 | 3.35 | 2.98 | 3.25 | 3.9 |
| $K_2O$ | 4.61 | 5.55 | 5.33 | 5.12 | 4.8 |
| $P_2O_5$ | 0.05 | 0.06 | 0.07 | 0.01 | 0.01 |
| rest | 0.12 | | 3.00 | 0.09 | |
| Total | 99.13 | 100.00 | 99.60 | 98.85 | 99.78 |

AB421, AB401: Klimm et al. (2008)

LBT, EBT: Hildreth (1979), Hildreth

and Wilson (2007)

52

9/1/2015

PX-LBT: average (n=25) of pyroxene-bearing LBT, from

Hildreth and Wilson (2007)

1153

1154

9/1/2015

1155    Table 2: Estimate of the bulk partition coefficient for Ti in the Bishop Tuff magma

| Mineral | Mode | D value $C_{Ti}$ in melt = 0.1 wt% | D value $C_{Ti}$ in melt = 0.2 wt% |
|---|---|---|---|
| *Quartz* | 0.42 | 0.1 | 0.1 |
| *Plagioclase* | 0.18 | 0.1 | 0.1 |
| *Sanidine* | 0.34 | 0.1 | 0.1 |
| *Biotite* | 0.03 | 50 | 25 |
| *Pyroxene* | 0.01 | 0.5 | 0.5 |
| *Ilmenite* | 0.0005 | 490 | 245 |
| *Magnetite* | 0.02 | 90 | 45 |
| **Bulk D** | | **~3.6** | **~1.9** |

1156    Mineral modes from Hildreth, 1977, Appendix XII. Partition coefficients (D value) of

1157    plagioclase, and clinopyroxene were taken from GERM database

1158    (http://earthref.org/KDD/). D values for sanidine and quartz were estimated to be

1159    similar to plagioclase. D values of biotite, ilmenite and magnetite were estimated

1160    using an average Ti concentration in the minerals from Hildreth, 1977 (5 wt% $TiO_2$

1161    in the biotite, 49 wt % $TiO_2$ in ilmenite, 9 wt % $TiO_2$ in the magnetite and ~0.1 or 0.2

1162    wt %$TiO_2$ in the melt).

1163
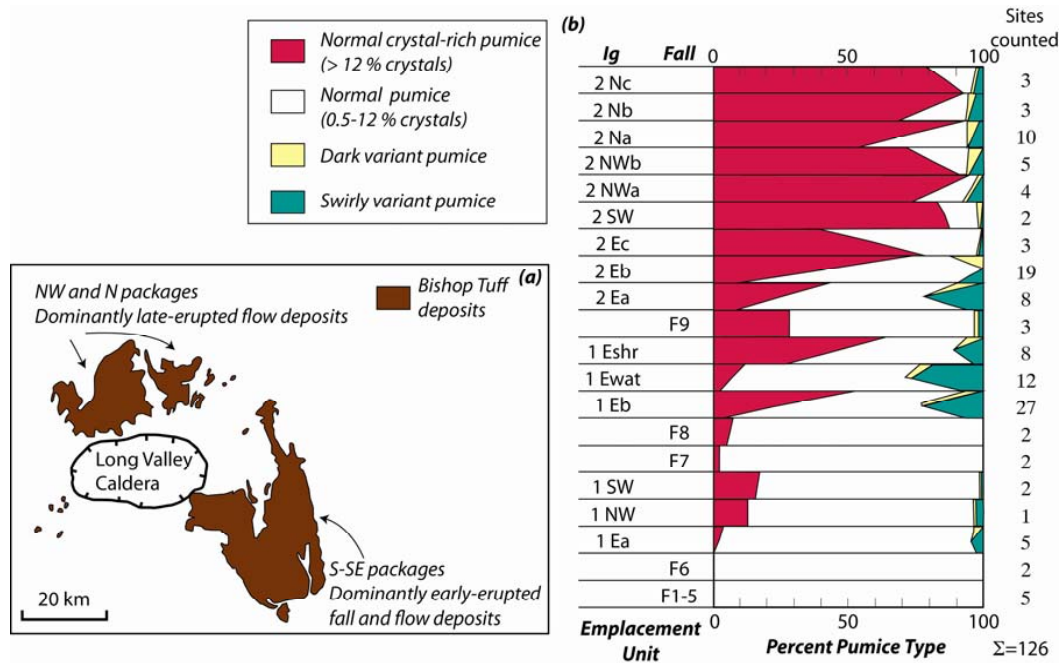
54

9/1/2015

1164



1165
1166    Figure 1: (a) Simpified map and packages of deposits in the Bishop Tuff. The SW cluster

1167    of glaciated remnants includes superimposed packages of both Ig1SW and Ig2SW. (b)

1168    pumice clast proportions of the different Bishop Tuff emplacement units. Diagonal lines

1169    indicate ranges in deposits. The succession of emplacement units (Ig, ignimbrite package;

1170    F fall unit) is detailed in Hildreth and Wilson (2007). Modified from Hildreth and Wilson

1171    (2007).

1172

55

9/1/2015

1173  **FIGURES**

1174
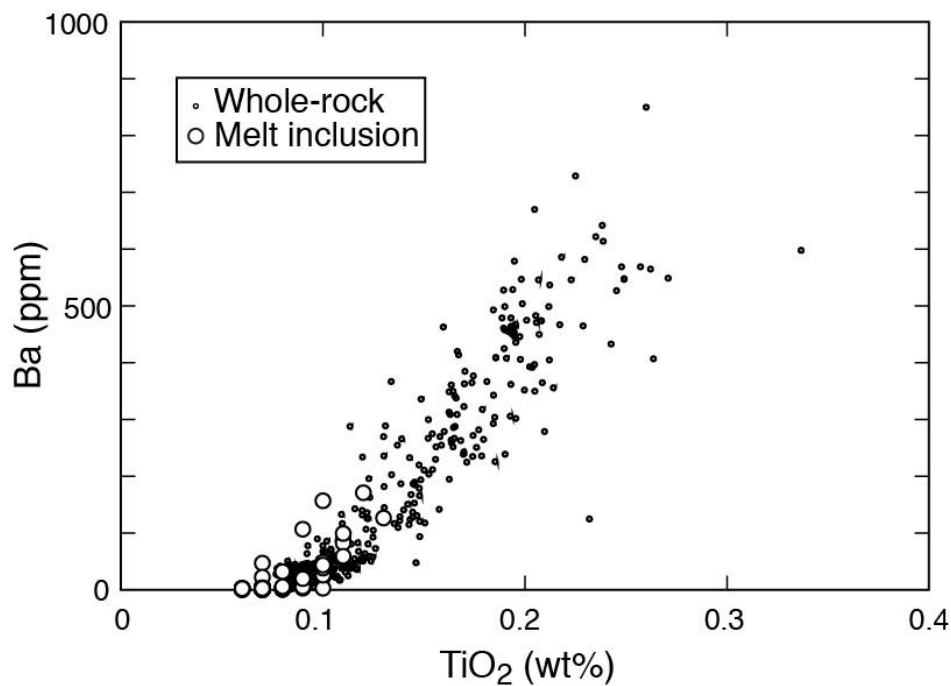


1175

1176

1177  Figure 2: Ba (ppm) vs. TiO$_2$ (wt.%) in Bishop Tuff pumices (whole-rock) excluding 4

1178  trachydacites and 2 dark pumices, from Hildreth and Wilson (2007, Appendix 4), and

1179  melt inclusions, from Wallace et al. (1999), Anderson et al. (2000), and Peppard et al.

1180  (2001). Note the similar trends but contrasting ranges in the two populations. Melt

1181  inclusion data are predominantly from CL-dark quartz interiors.

1182

56
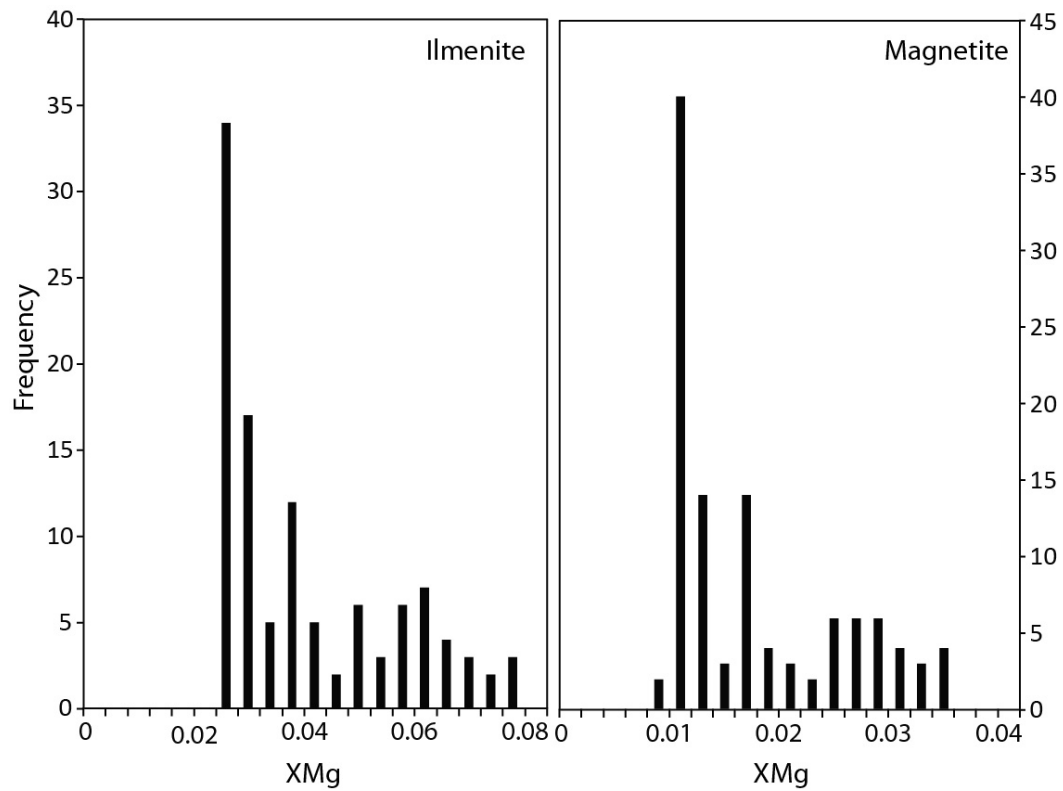
9/1/2015



Figure 3. Frequency histograms for $X_{Mg}$ in ilmenite and magnetite in the Bishop Tuff. Data from Hildreth (1977) and Hildreth and Wilson (2007, Appendix 3). This updates histograms in Gualda and Ghiorso (2013a) and Gardner at al. (2014). Data from sample BT129 were omitted because ilmenite in this sample contains 14% pyrophanite component, anomalously little Mg ($X_{Mg}$ =0.01), and is clearly out of MgFe-exchange equilibrium with its coexisting magnetite (Evans and Bachmann (2013, Fig. 2). It was probably vapor-phase modified (Hildreth and Wilson 2007, Fig. 15).
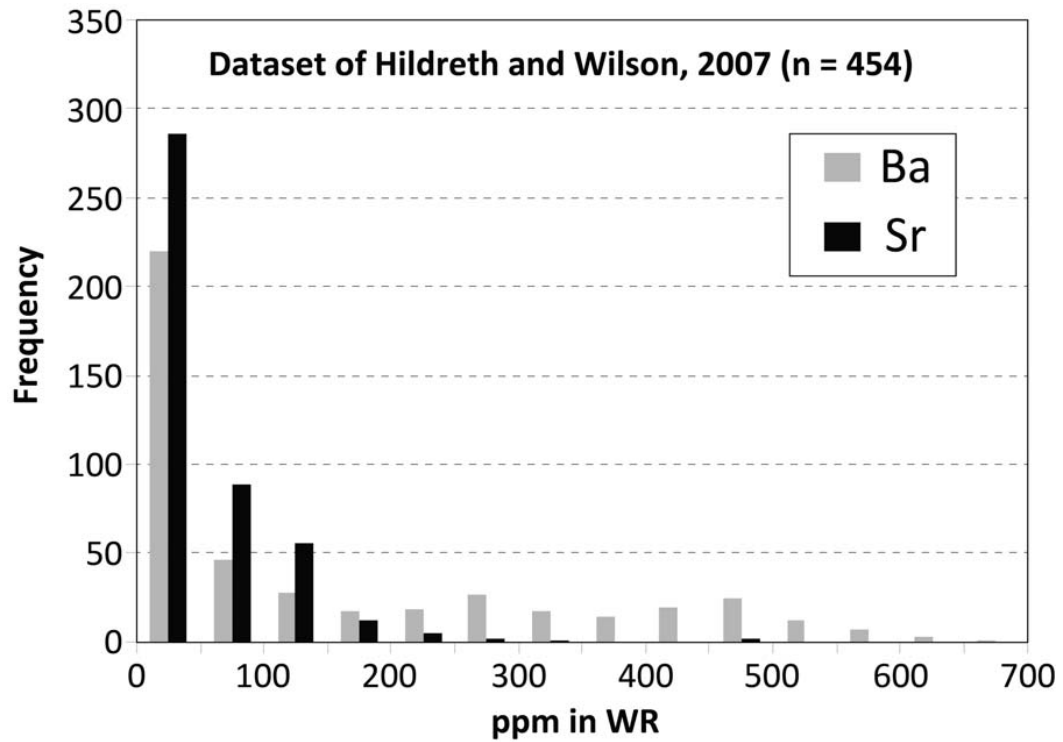
9/1/2015



1194

1195     Figure 4. Frequency histogram for whole-rock Ba and Sr concentrations in the Bishop

1196     Tuff. From dataset of Hildreth and Wilson (2007, Appendix 4).

1197

1198

9/1/2015
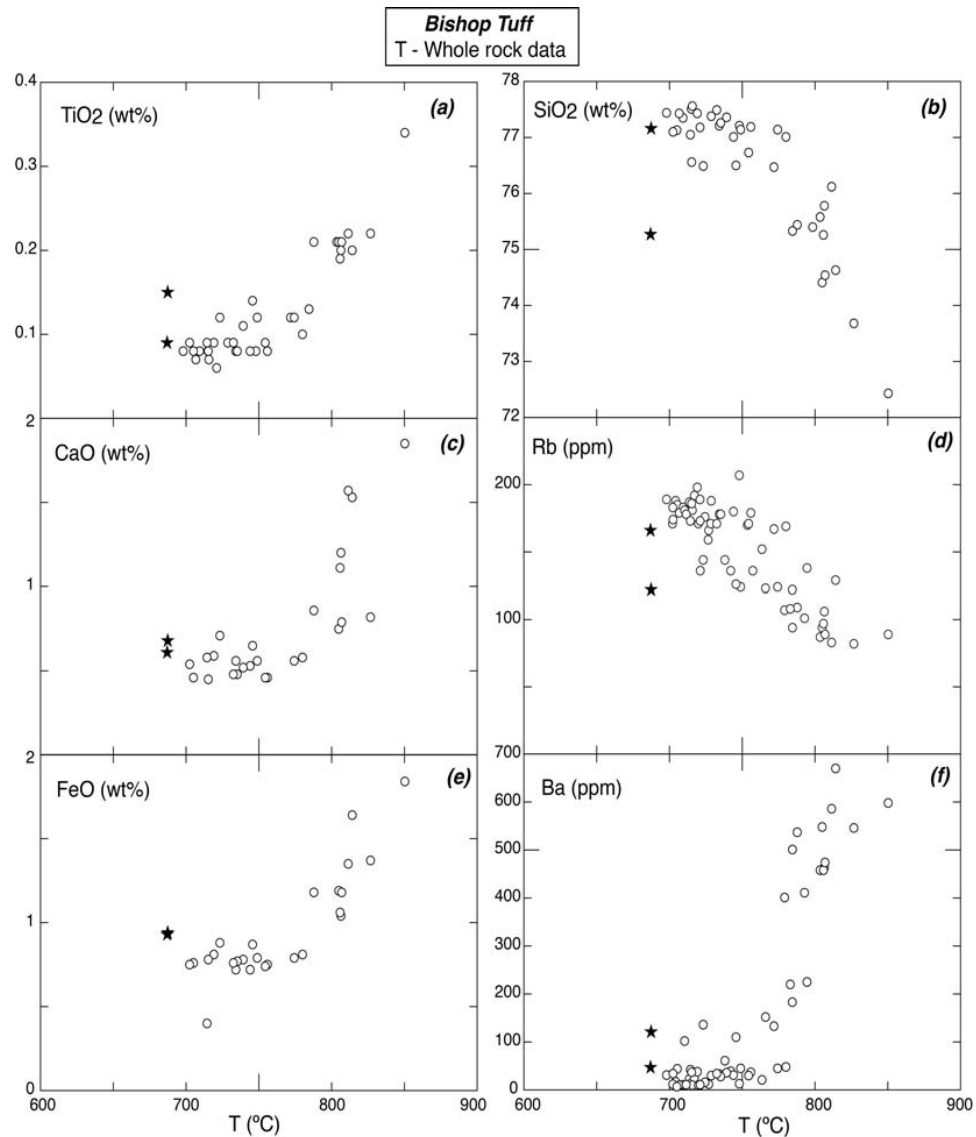


1199
1200  Figure 5. Correlation between FeTi-oxide temperature and whole-rock compositions for

1201  four compatible elements (a, c, e, f) and two incompatible elements (b, d) in the main

1202  array of the Bishop Tuff. Outlier samples B355B and B383B (stars) are inferred to have

1203  undergone post-depositional changes (Evans and Bachmann 2013, Fig. 1). Seven

1204  duplicate oxide pairs were averaged. Data taken from Hildreth (1977) and Hildreth and

1205  Wilson (2007, Appendices 3 and 4) and Ghiorso and Evans (2008).

1206

59

9/1/2015

1207

1208

1209

1210

1211

1212

1213

1214
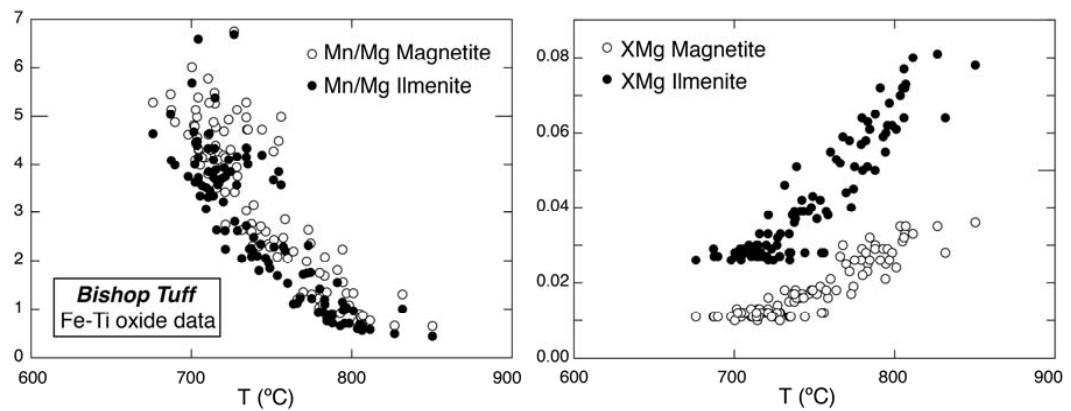


1215

1216

1217  Figure 6. Weight ratio Mn/Mg and atomic ratio $Mg/(Mg+Fe^{2+})$ of magnetite and ilmenite

1218  versus FeTi-oxide temperature for all analyzed pairs in the Bishop Tuff. Data from

1219  Hildreth (1977), Hildreth and Wilson (2007) and Ghiorso and Evans (2008).

60

9/1/2015
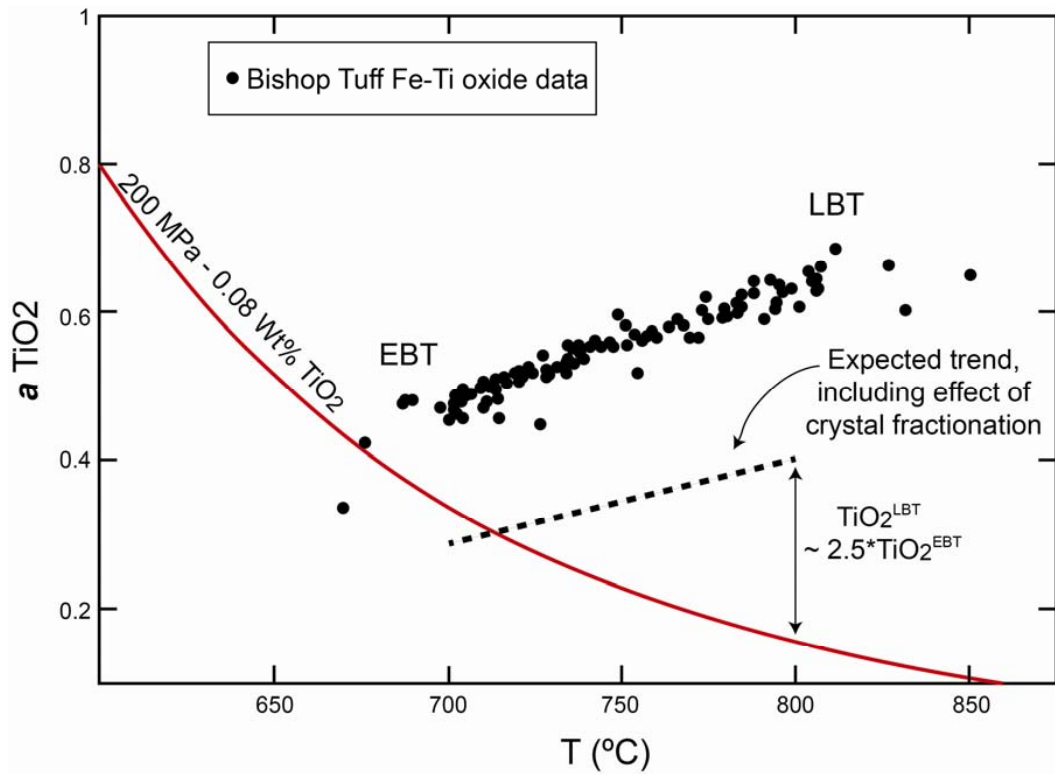


1220

1221

1222   Figure 7: Curve of $aTiO_2$ vs. $T$ at 200 MPa for a Bishop Tuff composition with 0.08 wt%

1223   $TiO_2$ and corresponding loci of the Fe-Ti oxides (dots), from Ghiorso and Gualda 2013),

1224   compared to the expected change in $aTiO2$ vs. $T$ (dashed line) assuming a difference of

1225   X2.5 in melt $TiO_2$ between EBT at 700°C and LBT at 800°C (see text for details).
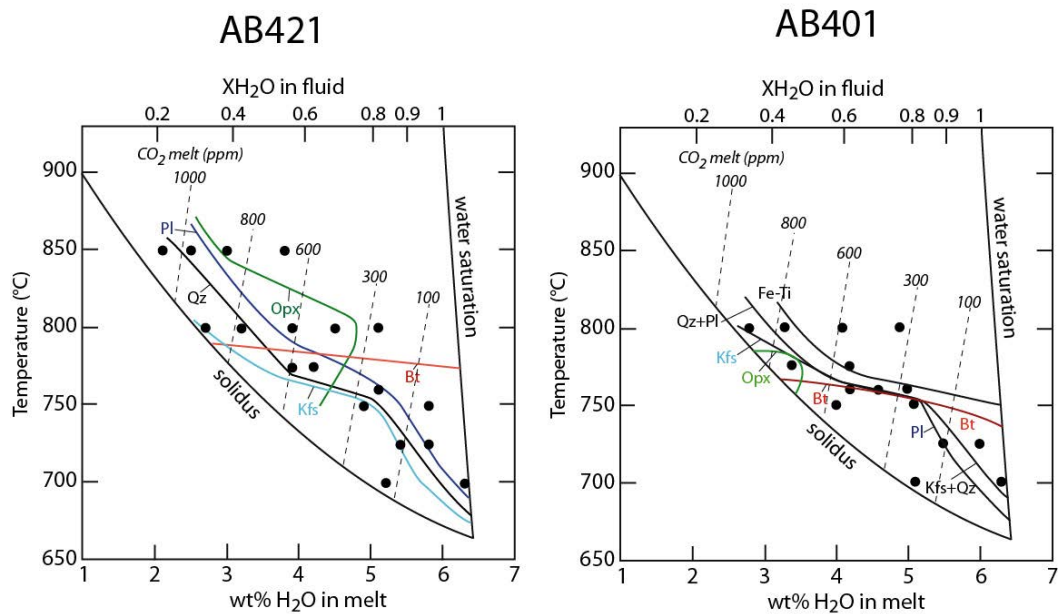
1226

1227

61

9/1/2015
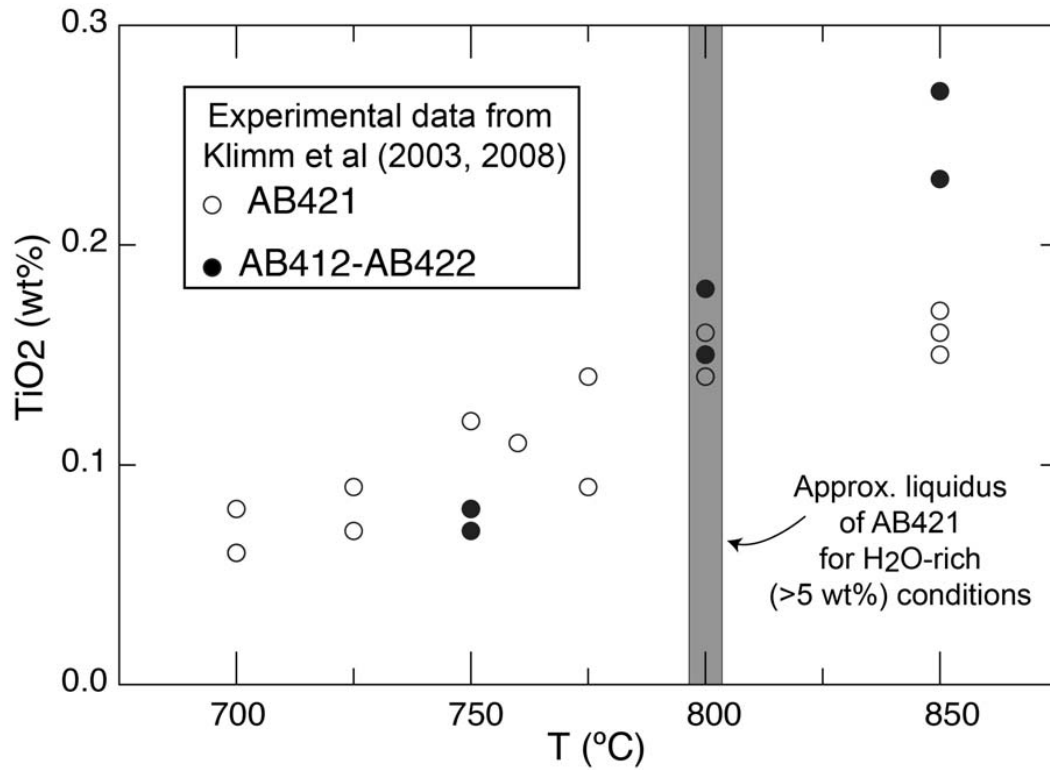


1228

1229

1230    Figure 8: TiO$_2$ content vs. *T* for high-silica residual melts saturated in FeTi oxides in

1231    high-temperature experiments on three fused granitoids (Klimm et al. 2003; Klimm et al.

1232    2008), showing the igneous compatibility of TiO$_2$ at   ΔNNO = 0 to - 1.0 (decrease of

1233    TiO$_2$ as a function of *T*).

1234

1235

9/1/2015



1236

1237    Figure 9. Experimental results for crystallization at 200 MPa of two fused leucogranites

1238    AB421 and AB401 (as proxies for average LBT and EBT rhyolites, see Table 1; from

1239    Klimm et al. 2008, temperatures determined by thermocouples), contoured for ppm $CO_2$
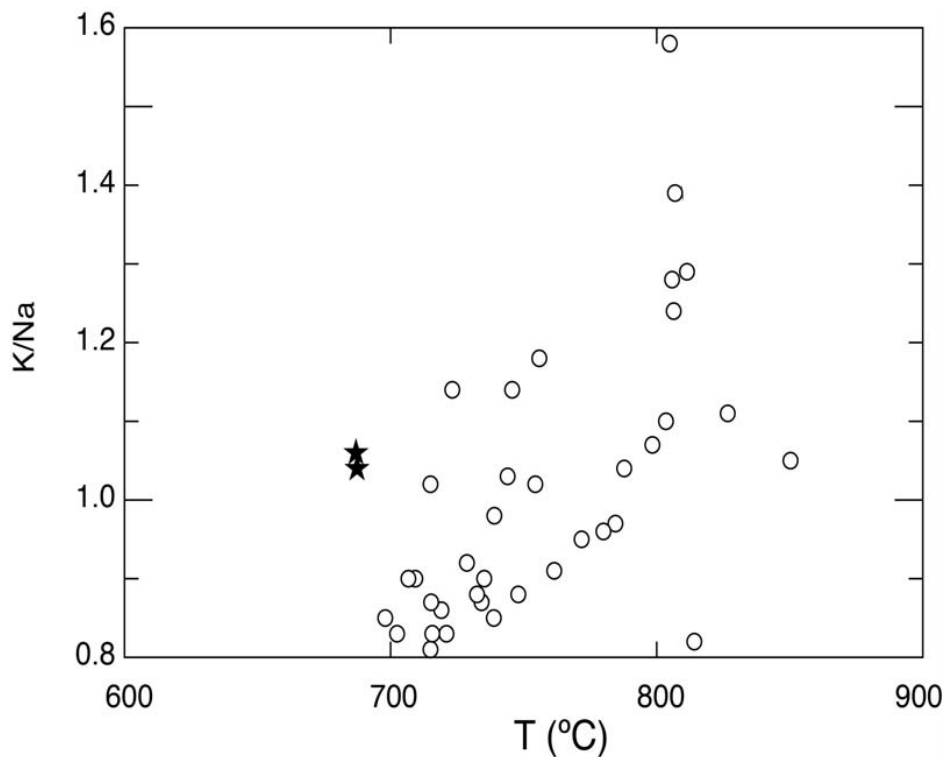
1240    in the melt.

1241

1242

1243

1244

63

9/1/2015



1245

1246    Figure 10.  Diagram showing that whole-rock samples of hot (LBT and EBT) Bishop

1247    Tuff have higher atomic K/Na than cooler (☐700°C) EBT samples. Some of the

1248    higher K/Na samples may have been altered by post-eruption hydration (see text).

1249    Stars: see Fig. 5 caption. Data from Hildreth and Wilson (2007).

1250

1251

1252